

1994

Application of the X-ray measurement model to image processing of X-ray radiographs

Elizabeth M. Siwek
Iowa State University

Follow this and additional works at: <https://lib.dr.iastate.edu/rtd>

 Part of the [Electrical and Electronics Commons](#)

Recommended Citation

Siwek, Elizabeth M., "Application of the X-ray measurement model to image processing of X-ray radiographs" (1994). *Retrospective Theses and Dissertations*. 255.
<https://lib.dr.iastate.edu/rtd/255>

This Thesis is brought to you for free and open access by the Iowa State University Capstones, Theses and Dissertations at Iowa State University Digital Repository. It has been accepted for inclusion in Retrospective Theses and Dissertations by an authorized administrator of Iowa State University Digital Repository. For more information, please contact digirep@iastate.edu.

**Application of the x-ray measurement model to image processing of
x-ray radiographs**

by

Elizabeth Maria Siwek

A Thesis Submitted to the
Graduate Faculty in Partial Fulfillment of the
Requirements for the Degree of
MASTER OF SCIENCE

Department: Electrical Engineering and Computer Engineering
Major: Electrical Engineering

Approved:

Signature redacted for privacy

For the Graduate College

Iowa State University
Ames, Iowa
1994

TABLE OF CONTENTS

ACKNOWLEDGMENTS	vii
CHAPTER 1. INTRODUCTION	1
Scope of Research	3
CHAPTER 2. X-RAY RADIOGRAPHY	5
X-Ray Theory	6
Detectors	10
Film	10
Real-Time Imaging	12
X-Ray Process Model	13
Capabilities	16
Applications	18
CHAPTER 3. DIGITAL IMAGING	20
General Image Processing Techniques	20
Digitizing Equipment	22
Dynamic Range	25
CHAPTER 4. MATCHED FILTER	33
Background	34

Results	37
Volumetric Flaws	37
Crack-like Flaws	45
Summary	46
CHAPTER 5. IMAGE SUBTRACTION	51
Calibration	52
Image Registration	56
Subtraction	60
Summary	65
CHAPTER 6. CONCLUSIONS	67
Future Work	69
REFERENCES	71

LIST OF TABLES

Table 4.1: 40

LIST OF FIGURES

Figure 2.1:	X-ray imaging.	8
Figure 2.2:	Geometric unsharpness.	9
Figure 2.3:	Photograph of automobile air conditioner compressor.	15
Figure 2.4:	CAD drawing of automobile air conditioner compressor.	15
Figure 2.5:	Radiograph of automobile air conditioner compressor.	17
Figure 2.6:	XRSIM output of automobile air conditioner compressor.	17
Figure 3.1:	Diagram of digitizing set-up.	23
Figure 3.2:	Density plot for light intensities at 10, 100, 1300, and 13000 footcandles.	27
Figure 3.3:	Density plot for light intensities at 25, 250, and 1600 footcandles.	29
Figure 3.4:	Digitized images at varying lightbox intensities. (a) Image at 25 footcandles. (b) Image at 250 footcandles. (c) Image at 1600 footcandles. (d) Combined image.	31
Figure 4.1:	Original image of flat plate with voids. The flaw sizes clock- wise from top left are 1%, 3%, 7%, and 5%.	38
Figure 4.2:	Filtered image of flat plate with voids. The flaw sizes clock- wise from top left are 1%, 3%, 7%, and 5%.	38

Figure 4.3:	Detection of voids in an aluminum weld. (a) Original image. (b) Matched filter result.	41
Figure 4.4:	Original image of an air-conditioner part.	43
Figure 4.5:	Filtered image of an air-conditioner part.	43
Figure 4.6:	Plot of flaw area. (a) Original image. (b) Filtered result. . .	44
Figure 4.7:	Model generated image with cracks.	47
Figure 4.8:	Filtered with passes at several different angles.	47
Figure 4.9:	Filtered image with thresholded images summed.	47
Figure 4.10:	Crack in weld. (a) Original image. (b) Filtered result.	48
Figure 4.11:	Image near bolt-hole. (a) Original image. (b) Filtered result.	48
Figure 5.1:	Density comparison of model output to measured values. . .	54
Figure 5.2:	Gray scale calibration for model output.	55
Figure 5.3:	(a) Original CT image. (b) Model generated image. (c) Sub- tracted image.	59
Figure 5.4:	Arbitrary cast part. (a) Model generated image with flaw. (b) Model generated image without flaw. (c) Subtracted image.	61
Figure 5.5:	Edge section of air-conditioner part. (a) Digitized radiograph. (b) Model generated image. (c) Subtracted image.	63
Figure 5.6:	Center section of air-conditioner part. (a) Digitized radio- graph. (b) Model generated image. (c) Subtracted image. . .	64

ACKNOWLEDGMENTS

First, I would like to thank the members of my committee, Dr. Joe Gray, Dr. John Basart, Dr. Jennifer Davidson, and Dr. Dick Wallingford; for helping and encouraging my research, every step of the way. I especially thank Dr. Joe Gray for the many years of friendship and academic support he has given me, especially during my graduate years. I also appreciate the help and cooperation of many individuals at the Center for Nondestructive Evaluation, including: Jason Ting, Rick Powell, Ed Doering, Troy Groth, Sarat Kakumanu, and Vivekanand Kini.

There are many other people who have helped me in non-academic matters, but who indirectly motivated the completion of this thesis. I'd like to name just a few of these great friends: Jim Zelle, Kathy Nutt, Linda Bailey, David Bixby, Greg Strabala, Jim Carter, and Rose Pence. My gratitude is also extended to Doug Pinnick, Ty Tabor, and Jerry Gaskill; none of whom will ever know how much they have inspired me. Last, but not least, I'd like to give a very special thanks to a very special person, Eric Daugherty...just because.

This work was sponsored by the NSF Industry/University Center for NDE at Iowa State University.

CHAPTER 1. INTRODUCTION

Information can be conveyed in many forms, yet it is perhaps easiest interpreted when in a visual form. The human mind has the ability to look at a scene containing complex patterns and extract particular features by considering the content of the entire image and focusing on the items of interest. The processing power, speed to decipher images, and complexity of the human brain has yet to be matched by any artificial means. Although the brain is an excellent processor and interpreter, a human can tire and become less accurate with time, potentially causing costly errors. Since consistency is especially important in inspection situations, it is desirable to automate part or all of the vision process to simplify the inspection. Thus, images can be acquired and processed to improve image quality for either human interpretation or machine perception and analysis. With image processing, it is possible to remove patterns or artifacts induced by the testing equipment, or to seek particular features for enhancement or extraction. The use of imaging technologies facilitates quantitative analysis and objective interpretation of selected parameters, especially in repetitive tasks.

In industry, analysis and interpretation of x-ray images are frequently required for nondestructive evaluation (NDE). Radiographs of parts are taken, then examined for any voids, cracks, or inclusions that may later propagate to cause failure of the

component. Film has historically been used as the detection medium in radiography because it has the advantages of high resolution, high dynamic range, and convenient archival. It remains the most common medium because it proves to be a valuable and cost effective means of quality control. However, the overall effectiveness of this technique can be improved by continuing to collect the data on film, then digitizing the areas of interest for analysis.

Once digitized, analog film images may be enhanced to change specific characteristics or the overall image. Over the last decade, imaging has become a broad topic used widely in a variety of scientific fields from medicine to remote sensing. Although the applications vary, the techniques for processing images remain similar. Many general image processing techniques have been developed which can improve image quality including noise suppression, trend removal, and edge detection. For specific needs, these processes can be combined to manipulate an image for enhancement or extraction of particular features of interest.

Although a number of processing tools may be used on a wide variety of applications, it is possible to tailor a tool for a specific function by utilizing the knowledge available for a particular situation. For this study, a focus on x-ray inspection at the production phase was chosen, because the part is still in a controlled environment, providing fewer variables. Specific knowledge is available about what the part is supposed to look like, what the critical flaws are, and where the part has been since its initial manufacture. Since the type of part in production is constant or has limited variability and the ranges of critical flaws are known, an automated detection scheme may be adapted for many situations.

Scope of Research

The work presented in this thesis takes image processing away from the general and into the specific. The application considered was the inspection phase of a production line. At this point, hundreds of radiographs may be examined daily for the same types of critical flaws. Often these parts in production are designed using computer aided design (CAD); therefore, a computer file for the part exists which describes the part's size and shape parameters. Utilizing this information about the part, along with its material properties and inspection criteria, application specific inspection techniques were developed.

An x-ray process model, XRSIM [12, 13, 14, 15], has been created which uses CAD information to simulate a film response to experimental testing. It was desired to utilize the information produced by this program to help analyze the images created for actual inspection. Since the testing would be done at a very controlled phase in the life cycle of the part, the CAD model and simulation data could be treated as a perfect part, allowing a comparison to the parts being tested. With this unique information in mind, two approaches which utilized XRSIM were examined. The first considered flaw characteristics and detection criteria and the second considered overall image enhancement to improve detectability.

The first method investigated is the use and effectiveness of the simulation code to generate optimal matched filter elements. Assuming the critical flaw shape and size are known, XRSIM could be used to design a filter with that flaw description. Using the filter on the image, the filter should ideally match and amplify the critical flaws. By using the simulation code, a wide range of morphologies can be examined and optimal libraries of filter elements can be assembled; however, one of the limitations of

the matched filter approach is the unknown variability of the actual flaw morphology.

The second method is the subtraction of a "simulated" x-ray image from a digitized radiograph to reduce the effects due to thickness variation in the sample. By eliminating the structural features of a part, flaws are revealed that are otherwise undetectable. The issue of spatial and gray scale registry necessary for subtraction of the images is also addressed.

A description of the background and details of this work is presented in the following chapters. Chapter 2 provides background information on the radiographic process and a description of the x-ray process model, XRSIM. Chapter 3 discusses general image processing techniques, the digitization process, and how the dynamic range of an image is maximized. Chapter 4 focuses on the matched filter technique. The effectiveness of this method on detecting volumetric and crack-like flaws is presented. Chapter 5 presents the details of using XRSIM for image subtraction. A summary of this work is presented in Chapter 6, which also suggests areas for further investigation.

CHAPTER 2. X-RAY RADIOGRAPHY

Radiographic inspection is one of the most common forms of NDE. A variety of nondestructive techniques have been developed to inspect parts without compromising their integrity. These methods are all designed to detect flaws in objects, yet they range in complexity from a simple visual inspection to laser-based techniques. The most common methods utilize radiography, ultrasound, eddy current, magnetic particles, and liquid penetrant. Newer techniques such as acoustic emission, thermography, and holography are also being used [19].

Most NDE techniques involve introducing a known signal into an object and analyzing the results for anomalies in the signal. These anomalies may indicate voids, cracks, or changes in material composition. For radiography, an x-ray beam is transmitted through an object and a pattern of the object, along with its anomalies, is projected onto a detector. Ultrasonic techniques work by projecting an acoustic signal into a solid object, which is reflected when it reaches an anomaly or flaw. Eddy current inspection involves supplying an electromagnetic field to a metal specimen and observing the interaction.

It is possible that several techniques may achieve the same end; however, one is chosen by its effectiveness and appropriateness to the situation. For example, ultrasonic techniques are effective for solid objects, but are difficult to use on objects

which have intentional gaps in the structure, such as honeycomb or wing spars. Eddy current techniques, although effective in detecting surface defects in metals, can not detect flaws far from the surface or in non-metal objects. Neither technique works well on parts with complex geometry, yet x-rays are ideal for such a situation.

X-ray inspection is an inherently visual NDE technique. Data for x-ray inspection is usually collected with a two-dimensional detector, typically film. Since the method does not require any physical contact with the part, almost any type of part can be inspected using x-rays. The method is quick and the data is easy to interpret because it is in image form. The flexibility of radiography makes it a good inspection tool for production work.

The following chapter presents an introduction to the physical process of x-rays. An overview of the nature of x-rays, their interaction with material, and the imaging process are presented. This serves as background to the x-ray process model, XRSIM, which is used as a tool for image processing in later chapters.

X-Ray Theory

X-rays are high energy electromagnetic radiation in the range of 1 keV to 1 MeV and as such are penetrating ionizing radiation [9, 19]. X-rays travel in straight lines, are invisible to the eye, and have a photographic action similar to visible light. Among all of the methods used to produce x-ray radiation, the most common are radioisotopes and bremsstrahlung. Radioisotopes are elements which produce single energy emission while bremsstrahlung is typically produced by commercial x-ray machines and results in a broad energy spectrum. In this study, bremsstrahlung x-ray quanta were used. These x-rays are typically generated when electrons are created by a

heated filament, then accelerated to high energies and bombarded onto a metal target; the abrupt deceleration upon collision produces the x-rays.

The bremsstrahlung spectra are energy dependent. The number of photons created is controlled by the voltage and current settings of the generator, as well as other generator characteristics, such as: inherent filtration, target material and spot size, focal spot size. The maximum energy is controlled by the voltage. The intensity of the beam is further affected by the radial divergence of the beam, which is the same number of photons being spread over a greater cross sectional area, as distance from the source increases. In summary, this final x-ray photon intensity at the detector is based on the radial distance of the object from the source (r), the penetrated thickness (ρ) of the object, the linear absorption coefficient (μ) of the material, the integrated intensity over the area of the source (Figure 2.1).

For x-ray inspection, an x-ray beam is produced and projected onto an object; depending on its material density and the atomic number of the constituent atoms, a percentage of the x-ray photons are absorbed or scattered by the object. The x-ray quanta that are not absorbed by the object fall on the detector. An image is produced on the detector which is proportional to the varying levels of photons that reach it. For example, more photons will be absorbed by a thick part than a thin part of the same material; therefore, less photons will reach the detector. For film, the thicker part will have a lower exposure and appear light in shade; conversely, the thinner part will appear dark.

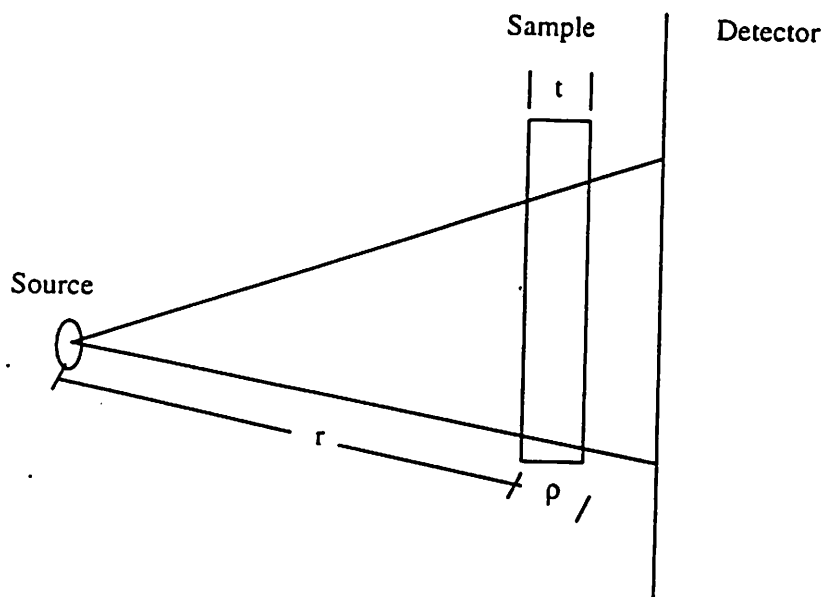


Figure 2.1: X-ray imaging.

Mathematically, the intensity of the beam reaching a particular location on the detector is defined as

$$I(x, y, E) = I_0(E) \int \frac{e^{-\mu(E) \rho(x, y)}}{r^2} dA \quad (2.1)$$

where, I_0 = incident intensity, *photons/cm²/sec*

ρ = thickness of material, *cm*

μ = linear absorption coefficient, *cm⁻¹*

r = distance from source to object, *cm*

dA = incremental area of the source, *cm²*

E = energy, *keV*

x, y = detector location

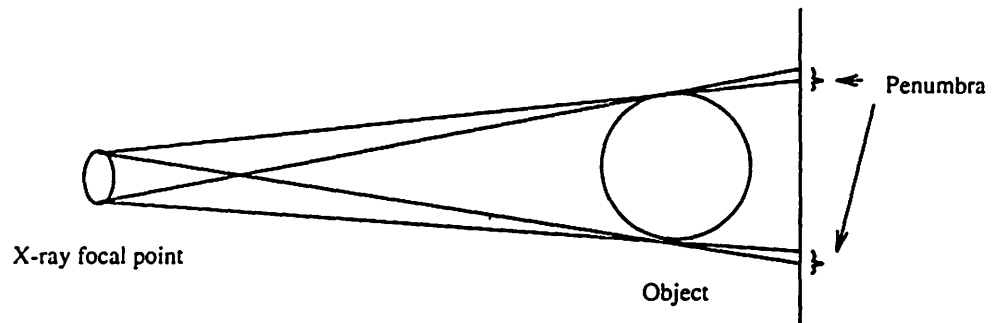


Figure 2.2: Geometric unsharpness.

An ideal x-ray source would be a point source; however, this is physically impossible. Typical x-ray sources have a focal spot on the target with a diameter of a few millimeters. In the early 1980's, microfocus sources were introduced, which have a focal spot of about 5-10 microns, which better simulates a point source.

Since the size of the focal spot is finite, it is an important factor in projection radiographic inspection. An effect directly related to the size of the source is the geometric unsharpness (U_g), or penumbra of the shadow. Rays originating from different points on the source will intersect the same point on the object at different angles. This will cause a point on the object to be projected to an area on the detector, in effect, blurring the image of the point. It should be noted that the U_g factor decreases as the source to detector distance decreases. This effect is illustrated in Figure 2.2.

Detectors

Film

Because of the high quality of the picture produced, and the archival nature of film; radiographic film is the most common detector used in industrial radiography. A radiograph is a photographic image produced after a beam of penetrating ionizing radiation passes through an object onto a film. When the film is exposed to x-rays or other electromagnetic radiation, a reaction occurs with the silver halide crystals within the film emulsion [9]. Upon development, the film darkens with respect to the degree of incident radiation. Intensifying screens can be used to increase the photographic effect of the film and to allow reduction of the exposure time. These screens, usually made of thin lead, are placed within the film cassette on either or both sides of the film. When excited by x-rays, the screens emit electrons, thus sensitizing the film and increasing the photographic effect. These screens also block out the scattering radiation, which improves the image quality.

The type of film holder used in experimentation plays a key role in the resulting radiograph. There are several types of film holders available, made from different materials. Some contain intensifying screens some do not. This should be taken into consideration when setting up an experiment because a standard film cassette with screens will give a much different result than paper, cardboard, or plastic cassette without screens.

The level of gray in a resulting radiograph can be quantified using optical density measurements, determined using a device called a densitometer. A typical industrial radiograph will have densities that range from 0-5. The measurement of density is

based on the intensity of the viewing light. Both the initial light intensity (I_o) and the transmitted light intensity (I_t) in the definition of film density are based on the light from the illumination used to view the developed film. This light intensity is not related to the aforementioned x-ray intensity. The optical density of the film is defined by [9]

$$D = \log_{10}(I_o/I_t) \quad (2.2)$$

The exposure of the film is based on the intensity (I_{x-ray}) and time (t).

$$E = I_{x-ray} * t \quad (2.3)$$

Inherent unsharpness, or film unsharpness (U_f), occurs when an x-ray quanta has sufficient energy to excite the crystals adjacent to the crystal initially sensitized. This causes a small blurring effect. The film and geometric unsharpness combine to equal total effective unsharpness (U_t),

$$U_t = U_g + U_f \quad (2.4)$$

where $U_f < U_g < U_t$, based on film sensitivity.

Film sensitivity is based on the grain size of the film. The smaller the grain size, the better the resolution. Yet, larger grain film requires a shorter exposure. The range of possible densities is also built into the film, with a limiting range. Where medical film may only reach the optical density of 3, industrial film has a larger range and will saturate around 5.

Noise can also be introduced into the image by the quantum mottle of the system. The quanta that compose the x-ray beam have a random statistical nature, thus may fluctuate over time causing variations [19]. This mottling effect can be compensated

for by using a longer exposure time for film, thus allowing an integration effect, which reduces the noise level.

Real-Time Imaging

Real-time imaging is an alternative to film. This method of x-ray detection is sometimes used in industrial inspection, where there is a high volume of parts that need to be inspected. The images created by real-time systems tend to have lower resolution and be noisier than film images, because the system has a lower dynamic range and creates the image instantaneously, not allowing time to integrate the noise. Because the sensitivity of the real-time system is much lower, it cannot be used in all inspection situations, yet it should be considered a viable alternative for future work.

A real-time imaging system consists of an image intensifier, camera, and a monitor. The image intensifier essentially converts the x-rays to visible light and increases the intensity of the image. The image intensifier consists of a phosphor screen, a light-to-electron screen behind it, a photo-multiplier, and an output screen. The entire apparatus is contained within a vacuum tube. The resulting image is then viewed using a camera, which is wired to the monitor. Depending on the system, the signal may or may not be passed through an imaging board on a computer. Some industrial systems are connected directly to the monitor, which limits the image enhancement capabilities to the analog adjustments available on the camera and monitor. An imaging board can capture an image, perform enhancements to better define the image, and save it in digital form, if required.

Several simple processing techniques, which are usually functions of the imaging

board, may be used to enhance the image quality. Frame averaging is used to factor out the background noise to obtain the optimum signal to noise ratio. Gain control can be used to increase the contrast of the image. A histogram of the image can easily be taken to determine the concentration of intensity levels in an image. Thresholding can then be done, so that the areas of interest can be emphasized. Arithmetic operations also may be performed on the image, as well as other enhancing techniques.

The digitization process electronically maps out the signal being received by the monitor. The signal is converted to a numeric code that shows the intensity level of each pixel on a 0-255 scale, where black is equal to zero and white is equal to 255. This digital form can then be used to extract information about the image.

There are several benefits of using this system. The most obvious asset is the speed at which an image can be produced, which is substantially faster than the time required to process film. Another advantage is that the position and orientation of the object being examined can be adjusted using the positioner while viewing the image. Also, the settings of voltage and current may be adjusted to study samples of varying thickness. The disadvantages of this system are the limited dynamic range, high level of noise, and low resolution of the images.

X-Ray Process Model

A computational model has been developed by other investigators, which simulates the film response from the interaction of x-rays with a sample [12, 13, 14, 15]. The number of photons which reach the film is based on the thickness of the part, part geometry, and the material absorption coefficient. Also taken into consideration are the x-ray beam characteristics, film properties, and the experimental configu-

ration. Scattering is accounted for by using a Poisson noise distribution, based on the film type. By using a solid model generated from a CAD package as a virtual part, film densities of the radiograph are predicted. The result of this simulation is a two-dimensional numerically generated digital "radiograph" of the part, which can be used to analyze the flaws in an actual radiograph with the same set-up and exposure parameters.

The model-generated images can vary in size and resolution, depending on the chosen parameters. For convenience, most of images used in this work were 256x256 pixels, with the features of the simulated images resolved to approximately match the size of the digitized radiograph under analysis.

For example, Figure 2.3 shows a photograph of a part from an automobile air-conditioner compressor. This part was chosen because it represents a typical production product. It is a cast aluminum part, which is subject to shrink porosity that may lead to failure of the part. This part also has several different thickness, which make it difficult to inspect with just one radiograph. Its dimensions are approximately 4 inches in length, 1 inch in diameter, and 0.25 inches at the thinnest portion. The part not only has thickness variation, but exhibits complexity of shape which makes it more difficult to inspect.

The design of this part is also typical of a component that might be produced by a computer aided design process. However, since a CAD model did not previously exist for this part, calipers were used to measure the dimensions of the part, then the dimensions were used to create a CAD model. The resulting modeled part is shown in Figure 2.4 and compares quite well with the original part.

As an experimental radiograph can be taken of the actual part, XRSIM can be

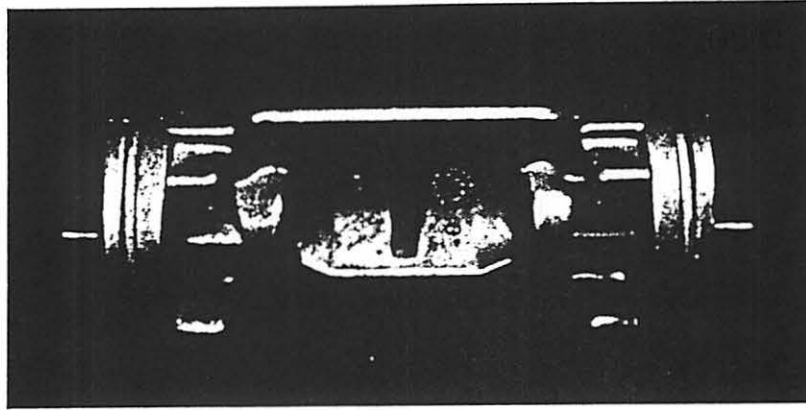


Figure 2.3: Photograph of automobile air conditioner compressor.

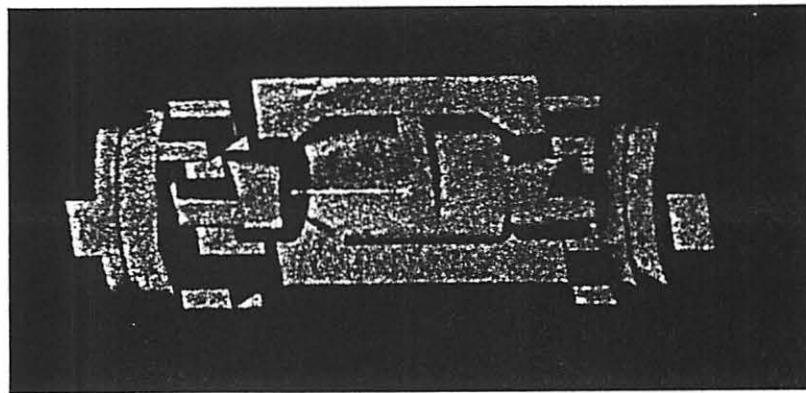


Figure 2.4: CAD drawing of automobile air conditioner compressor.

used to produce a digital radiographic image of the virtual part. XRSIM uses the CAD solid model and the material properties of the part to generate an image based on experimental settings. Figure 2.5 depicts a digitized version of an experimental radiograph of the real part, which has been slightly enhanced to show all the features. This can be compared to the output of XRSIM shown in Figure 2.6.

In comparing the digitized and model generated radiographs, it should be noted that the geometric features of the simulation output appear somewhat more square than its real counterpart. This is due to the CAD model representation of the part. Since the CAD model used was not the design model for the part, but was created by measuring and coding the dimensions, there are some slight inaccuracies in the shape. The sharp edges may also be attributed to the CAD model; however, since the part was cast, it would more likely have rounded rather than square edges. These features can be adjusted by refining the CAD model.

Capabilities

The modeling program, XRSIM, was written to effectively simulate the x-ray process using viable parameters and realistic settings. The program is based on both physical properties of x-rays and experimental data collected that demonstrate the limits of a system.

Since it was a goal to place XRSIM in a realistic setting, several variable parameters are available to customize the generator settings for a particular system. The spot size and shape of the x-ray source may be specified to simulate a broadfocus or microfocus machine, with the appropriate ranges for energy settings.

The experimental configuration can also be set. In addition to choosing the

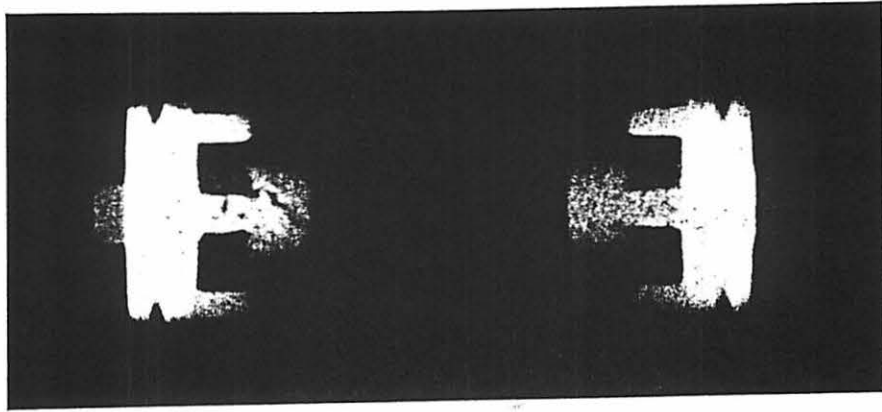


Figure 2.5: Radiograph of automobile air conditioner compressor.

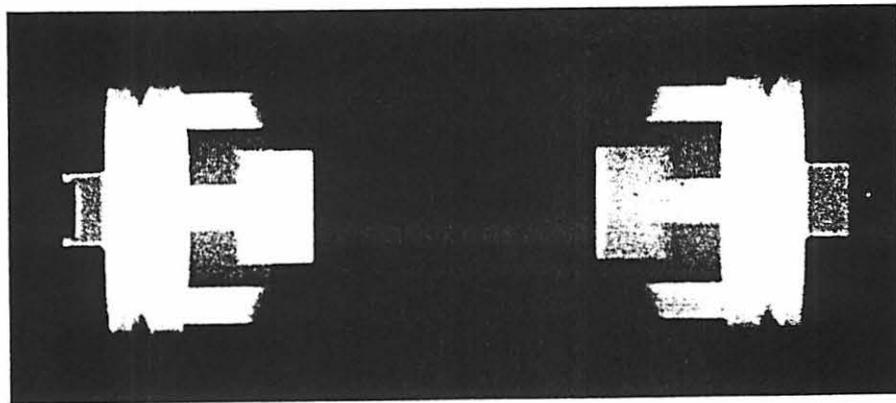


Figure 2.6: XRSIM output of automobile air conditioner compressor.

generator parameters, the locations of the sample and detector, sample material, and film type are also set. Although film is currently the only detector type available in XRSIM, a tomographic and real-time simulation package are under development [12].

For the selected parameters, the film response is determined based on the interaction of x-rays with the sample, while taking into account the material absorption and distances. The effective contribution of coherent, photoelectric, and Compton interactions are calculated for the selected energy. The film noise is modeled using a Poisson noise distribution for the random photon counting process. Film graininess is based on the film selection and modeled using a correlated Gaussian distribution. The noise in the model can be turned off to simulate a radiograph taken under ideal conditions.

In addition to producing accurate radiographic simulations for a particular modeled part, a flaw may be placed within the part. Conical or ellipsoidal shaped flaws may be sized and placed at any desired location. This allows the flexibility of modeling voids or cracks of many different shapes and sizes.

Applications

The x-ray measurement model was originally written to be used as a tool for predicting the limits for flaw detectability under specified circumstances. Since many components are designed using a CAD package, the idea of linking this initial design tool to final inspection was used as a basis for the model [4, 17]. By simulating an inspection at the design stage, an analysis can be made to determine the smallest detectable flaw. Throughout the design process the model can be used to reinspect the part, including any modifications that are made, without actually putting forth

the material and production cost of manufacturing a prototype.

As part of this iterative process, optimum inspection parameters can be determined to provide the best cost effective settings for inspection. The nature of the program allows several exposures to be taken to find the best contrast resolution. This feature also facilitates the training of operators. There are several other possible applications for XRSIM, two of which are examined in this thesis. These applications are very different from each other in nature, but innovatively utilize XRSIM for their purposes.

Two image processing techniques are considered which use the results of XRSIM as a base. Utilizing the known inspection set-up in a production situation, x-ray conditions can be modeled and radiographs simulated. The processing techniques then use the information contained in simulation results as a key to detecting flaws in the actual radiographs.

In one technique, the flaw feature of XRSIM is used to predict specific flaws in a part. With the inspection criteria known, the predicted flaw is easily modeled within the part. The flaw portion of the resulting simulation radiograph is then used as a template to locate flaws within the actual inspection radiographs. If the filter with the flaw signature directly matches a portion of the inspection radiograph, the signal would be amplified and the flaw located.

The other method used the simulation results as an ideal part. The actual radiograph was then compared to the ideal radiograph, produced by the XRSIM, by subtracting the ideal image from the real image. Since the two images represent the same part under similar inspection conditions, the subtraction process has the effect of canceling the similarities in the images and enhancing the anomalies.

CHAPTER 3. DIGITAL IMAGING

Over the last decade, imaging has become widely used in a variety of applications. It is common to apply image processing techniques developed in one field to another field. These techniques become more useful when adapted to a specific situation. For processing x-ray radiographs, it is important to consider the techniques available, the details of digitizing, and the information available within the image. Some background on these issues is presented in this chapter.

General Image Processing Techniques

Image processing techniques from scientific application areas such as medicine, astronomy, and remote sensing have been adapted for x-ray processing. The goal of all these general enhancement techniques is to enhance the appearance of the image without introducing artifacts. In radiographic images, it is desired to extract flaw information by either enhancing the feature of the flaw or suppressing the noise and background trends which obscure it.

Techniques such as background subtraction or contrast stretching are simple methods of improving the contrast of an image. Background subtraction removes the standard features which are continuously present, thus enhancing the objects of interest. Contrast stretching redistributes the intensities of the image, so the range of

possible gray levels is completely used. However, these methods are not as effective if the image has a full dynamic range of gray levels or has low signal to noise.

Histogram equalization is used to obtain a uniform histogram for the image. This process spreads the recorded values over the entire range of gray levels in such a way that every intensity level occurs with equal probability. This has the effect of increasing the contrast between consecutive intensity values occurring with higher probability.

Contrast can also be enhanced by amplifying large changes in the gray level gradient. Discrete methods used to measure gradient information are commonly referred to as edge detection techniques, since they emphasize the large gradients occurring at the edges. Classic spatial operators, such as Sobel and Laplacian, are often used in edge detection. The Sobel operator computes the gradient in the x-direction then y-direction and the Laplacian is a second derivative operator [20]. Both of these techniques can be simplified by considering them as masks which are convolved with the image.

Another method for edge detection uses moments to find the edges [21]. This is done by considering each intensity value as a density, then computing the center of mass. Once this point is located, the edges may be found vectorially outward from it.

Median filtering is not an edge detection technique; however, it is an effective nonlinear method of removing noise from an image. This smoothing method is sometimes used as a prefilter for edge detectors or basic image processing applications, such as background subtraction and thresholding [2]. The algorithm for median filtering replaces the gray level of each pixel by the median pixel value of the neighborhood.

Mathematical morphology is another technique which is used to extract flaws. Morphologic processing is the analysis of structure or texture. By analyzing the relationship between the intensity of the flaw and its surroundings, it can be done to extract the flaw.

All of these techniques may be applied individually to improve either enhance the overall image quality or in detecting flaws in radiographs; however, none of these techniques are specific for x-ray radiographs. It is possible to utilize the nature of x-ray radiographs to create a technique which is specified for radiographs alone.

Digitizing Equipment

In order to process or enhance an x-ray radiograph, it is first necessary to digitize it. In digitizing, discrete samples of the film are taken, with the location is represented by a corresponding pixel. Each pixel is assigned a gray level value based on the intensity of the transmitted light from each location. Although laser-based techniques are available for digitizing x-ray film, they are quite costly. It is more common to digitize radiographs using a computer based image acquisition system as shown in Figure 3.1. This system consists of three main devices: a light box, a video camera, and a frame grabber installed in a computer.

For both viewing and digitizing, it is necessary to illuminate a radiograph, so that it has proper contrast and its features are apparent. Care must be taken in selecting a light box with a fairly uniform illumination, so that it does not induce a varying background upon digitization. Variable brightness control is also desirable to enable viewing of film of different film density ranges. However, most variable

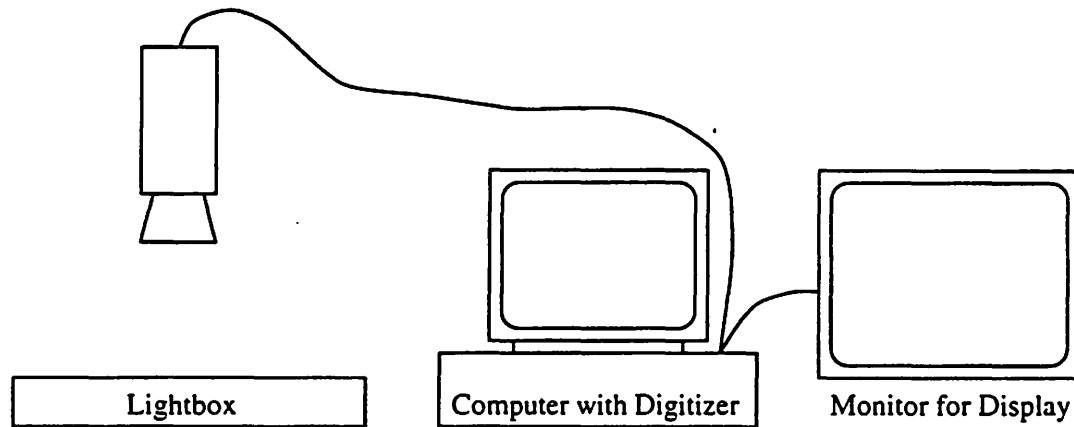


Figure 3.1: Diagram of digitizing set-up.

control lightboxes are manufactured for medical film viewing and do not reach the intensities necessary to illuminate high density industrial radiographs. In such cases, it may be necessary to utilize an alternate light box with a high intensity, but lower uniformity.

As your eye would capture an image and send it to your brain, a camera is a necessary input device to the computer. There are three main types of cameras that can be used for digitizing: tube, CCD, and CID. Tube cameras are an older variety, for which a vidicon or neuvicon tube is used to image the film and create an analog signal. A CCD (charge coupled device) camera directly captures the image in digital form on an array, with its resolution is determined by the size of the array. A CID (charge induced device) camera, works like a CCD camera but is different in the way

the data is read out. These cameras vary in complexity and may optionally have controls to adjust the gain, black level, or gamma. The gamma setting varies the compression of white values to improve low contrast images.

This image input is then sent to a frame grabber, which captures the image and translates the camera signal to a digital form for the computer. It takes approximately 1/30 of a second for a frame grabber to acquire a frame from a camera. The digitizer maps the voltages to corresponding gray levels, which are the pixel values in a digital image. The number of gray levels is dependent on the camera. An 8-bit camera most typically will produce 256 gray levels. Electronic noise may be introduced by the equipment, but this effect may be reduced by averaging together several frames. Frame averaging will also minimize fluctuations that occur in the lightbox illumination over time. The spatial distribution of the illumination of the lightbox and the level of room lighting also cause variations in the digitized image, but these effects can be minimized by choosing a uniform section of the lightbox and having the room as dark as possible at digitization.

With these basic components, imaging systems can be configured in many different ways. A wide variety of cameras and digitizing boards exist, with varying levels of adjustable features. This allows for greater flexibility in digitizing; however, the additional variables such as variable intensity lightboxes, aperture settings, gain controls, and gamma settings of the equipment add complexity to the process and make repeatability difficult once the settings have been changed. The positioning of the radiograph with respect to the camera can also be difficult to repeat, if the camera height changes or if a different area of a non-uniform lightbox is used.

The digitizing equipment used for this work consisted of two variable intensity

lightboxes, a Dage-MTI Series-70 camera with a neuvicon tube and a 35mm macro lens, and a Matrox Imager-AT digitizing board. One lightbox was an Aristo 1720 lightbox with a uniform variable light that could reach approximately 320 footcandles in brightness. The other lightbox from S&S X-ray Products could reach a brightness of 13000 footcandles, but had a less uniform field. The camera had analog controls to adjust the gain, black level, aperture, bandwidth, and gamma of the image. The imaging board also had gain and offset adjustments for the incoming image. For most cases, the settings on the equipment was left constant, except for the camera aperture, camera height, and lightbox intensity.

Dynamic Range

In working with the images, it was found that the digitization process was vital in having good images for processing. If the digitized image did not have sufficient dynamic range, the data would be insufficient to work with. For most digitizing systems, the dynamic range of the system is limited by either the camera or the digitizing board. Most systems are 8-bit, which means that there are 2^8 or 256 discrete gray levels to represent the radiograph. Unfortunately, the detail captured in the thousands of gray scale levels by the halide grains on a sheet of radiographic film, cannot be reproduced accurately in an 8-bit copy of the image. There are 12, 14, and 16 bit cameras that will increase the number of gray levels to 4096 or more; however, these systems are costly.

To improve the quality of the acquired image, adjustments are often made to enhance the dynamic range of the image before digitizing. By creating the best possible image at the time of acquisition, more can be done in the processing. Adjustable

variables in image acquisition include the light box intensity, camera lens aperture, camera gain and black level adjustment, and frame grabber gain and offset. Each of these parameters have some impact on the resulting image, but the parameter with the most significant effect was the light intensity level from the lightbox. The light box intensity controls the level of illumination of the radiograph, hence the range of gray levels that would be digitized. The gain of the camera also has a large effect because it controls the gray scale distribution upon digitization.

Although these adjustments may create a decent looking image, the image may still be lacking information in the areas of interest, due to the limited number of gray scales. It must be kept in mind that the computer processes information slightly differently than our brain. It will retain the differences between two shades of gray, that even our eye cannot distinguish; however, it may not pick up the subtleties that a human may distinguish by observing the entire area of the image. Hence, regions of film that may appear uniform to our eye, may actually contain many different optical density levels that the camera could distinguish.

To take advantage of the sensitivity of the camera, it is possible to concentrate on one area of interest when digitizing. This is useful when radiographs are taken of objects with several different thicknesses, which have corresponding variations in shades of gray. In taking one digital image, information may be lost due to the dynamic range limitation of the image capturing system. By varying the intensity of the lightbox one step at a time, several areas of interest may be properly illuminated, yet the other portions of the same radiograph will be too bright or too dark. However, combining images made with different lightbox intensities can effectively increase the dynamic range.

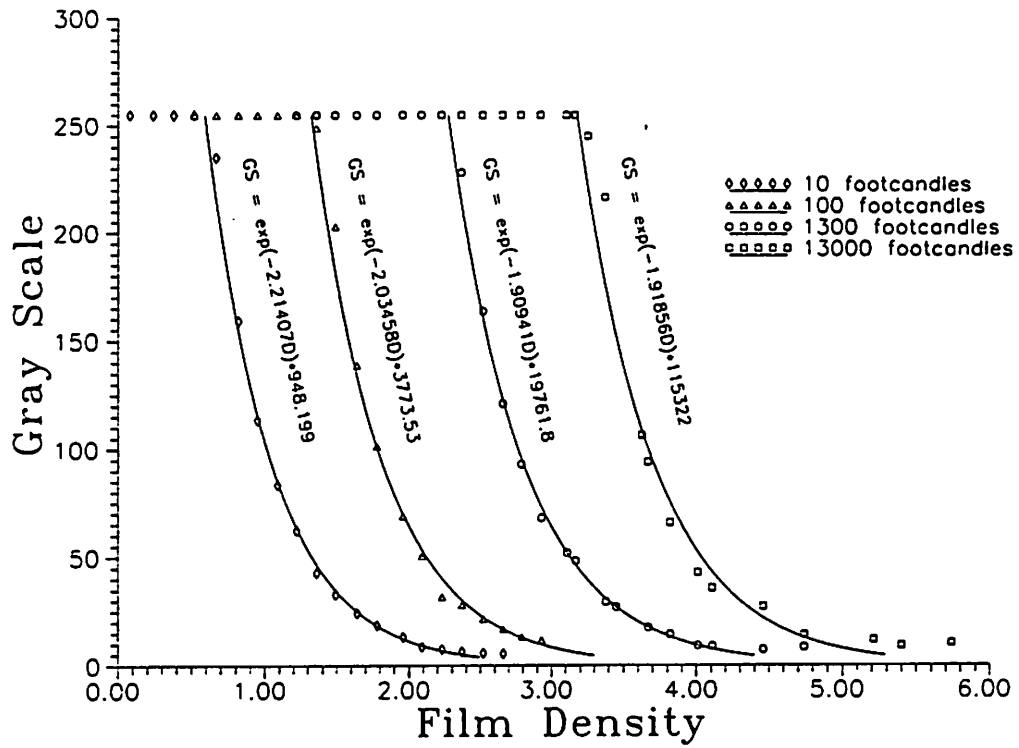


Figure 3.2: Density plot for light intensities at 10, 100, 1300, and 13000 footcandles.

The intensity of the lightbox dictates which portion of the optical densities on the radiograph are represented in the dynamic range of the gray scale. To show the limitations of the 8-bit camera, optical densities of radiographs were measured then digitized at different lightbox intensities, holding the other variables constant. Sample radiographs that spanned the 0-5 density range and clearly showed a step progression in density values were chosen so that a clearly defined area could be measured with both the densitometer and the imaging system. Figure 3.2 shows a graph of measured optical densities vs. the gray scale values upon digitization. Corresponding equations for the values were found by fitting curves to the data and are shown on the graph. In the equations, GS represents gray scale and D represents optical density. The digitized images acquired at each of these levels can be mapped into a larger range for subsequent manipulation. Images acquired at each of these levels show different features in the radiograph.

To exemplify the different variable settings, a radiograph of the part shown in Chapter 2 was digitized at different levels, then combined. The lightbox intensities shown in Figure 3.2 could not be used in this case, because the low intensity did not sufficiently illuminate any measurable values on the radiograph and the high intensity saturated the image of the part. Three light levels were chosen which revealed different features of the part and spanned the density range of the radiograph. Using reference radiographs, density and gray scale data were collected at each of these levels in the manner previously described. The plotted data is shown in Figure 3.3, with the corresponding equations noted on the graph. The importance of the choice of gain on the frame grabber is illustrated by comparing results from Figure 3.2 and 3.3. The slopes of the curves are too sharp for the gain setting in Figure 3.2, requiring

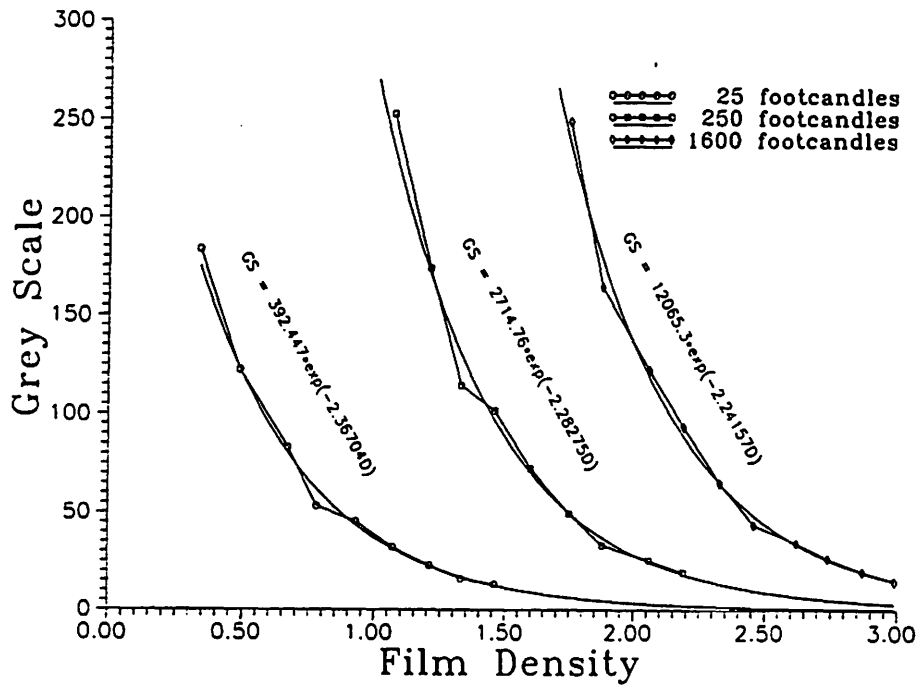


Figure 3.3: Density plot for light intensities at 25, 250, and 1600 footcandles.

a larger number of curves. A different choice of gain result in the three slopes in Figure 3.3.

Using these new digitization parameters, the radiograph was then digitized at each of the three selected intensities. These images are shown in Figure 3.4. At a low light level, 25 footcandles, details in the thicker portion of the part are apparent, while the thinner portion is is not sufficiently optically illuminated. In the intermediate exposure, 250 footcandles, the light saturates the portion of the film representing the thicker part, but reveals more of the darker portion of the film. On the brightest exposure, 1600 footcandles, details in the thinnest portion of the part are seen.

After digitizing the images, the gray scale values were mapped back to optical density values, using the equations found experimentally. Thresholds were set to remove the high and low values of each range and the component images were stretched to range from 0 to 255 for display purposes. This scaling was necessary because the combined data creates a larger dynamic range than the 8-bit monitor will display. An option to this scaling is to use a 16-bit image viewer. The combined image shows that a full range of information can be extracted from one image. Figure 3.4 shows the results of combining the images. The edges apparent within the combined image are possibly due to the intermediate scaling effect, a moderate margin of error in the calibration equations, or misregisty of the component images.

This technique is more useful if the component images are combined to create one image with values corresponding to the original optical densities and ranging from 0-5. Image processing can then be done on the newly created image, which contains the radiographic information in a larger dynamic range of density values. This potentially leads to a reduction in cost, because it reduces the number of film

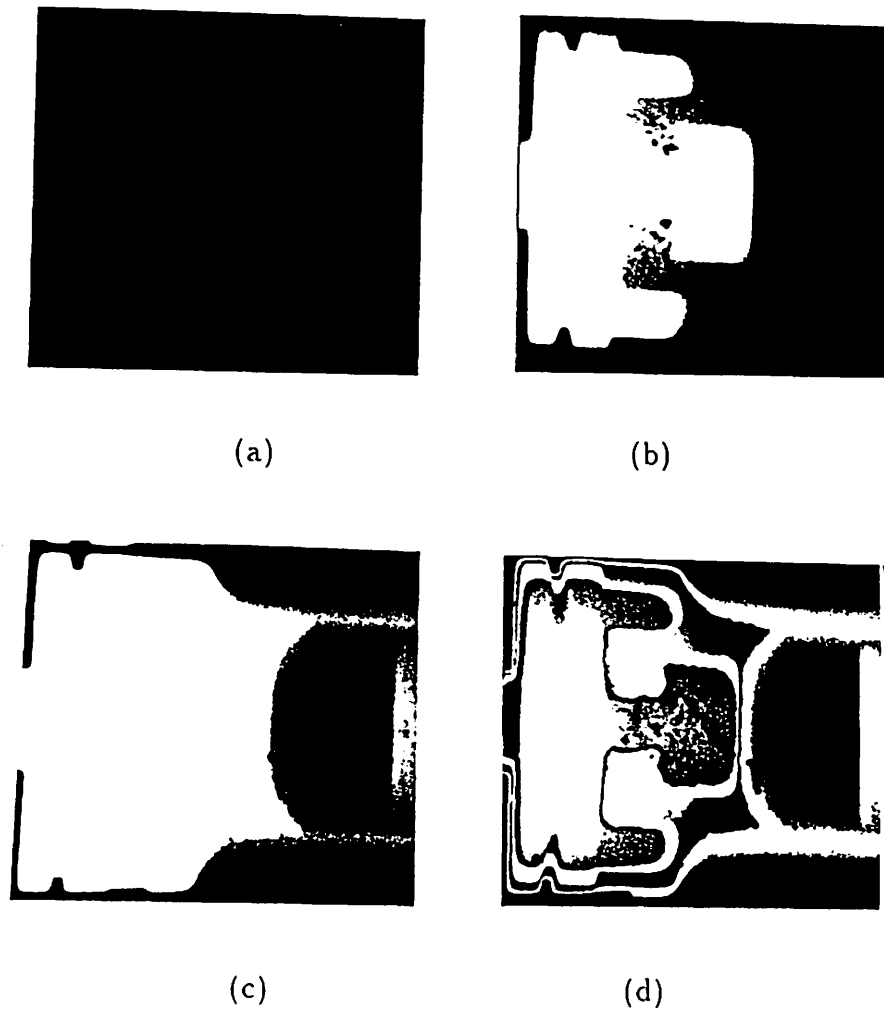


Figure 3.4: Digitized images at varying lightbox intensities. (a) Image at 25 footcandles. (b) Image at 250 footcandles. (c) Image at 1600 footcandles. (d) Combined image.

exposures necessary to inspect the part.

This information on digitization and dynamic range is important to consider when processing images. Maximizing the amount of information initially collected will increase the effectiveness of the processing techniques. Details of digitization also become relevant when comparing the digitized image to images produced by other means. This factor is further discussed in Chapter 5.

CHAPTER 4. MATCHED FILTER

Although classic image processing techniques, such as contrast stretching or histogram equalization, are sometimes used to enhance images for the detection of flaws, they may not be completely effective if the image is noisy. It is suggested that using a matched filter would be a more suitable technique for finding edges or flaws in high noise images [22]. The matched filter is used as a template to extract specific information from an image. The filter is passed through the image and produces a high signal response when the filter correlates, or matches, a particular portion of the image.

Flaws can come in many shapes and sizes, but are typically classified as either cracks or volumetric flaws, such as voids or inclusions. For radiographic images, the exact flaw characteristics are not always known, but can be approximated. Inspection specifications often provide information regarding the shape and sizes of critical flaws. Information concerning physical flaw characteristics, such as shape, size, and orientation of the flaw can be utilized to design a filter for a particular inspection need. When these three parameters are properly defined, the matched filter is a very successful feature extraction technique.

For this study, the effectiveness of two-dimensional matched filters used to detect and enhance the flaw signals in radiographs is examined. Both volumetric and

crack-like flaws in images are tested for detectability. Practical examples are used to determine the feasibility of this technique in realistic applications.

Background

Matched filtering can greatly enhance the signal to noise ratio (SNR) of a radiographic image. The theory has been presented in great detail by Turin [29, 30]. Matched filters have been widely used in a variety of applications including radar, sonar, photographic processing, and fingerprint matching [24]. More recently, this technique has proven effective for border detection in medical images [7]. Also, the edge recognition capability of matched filters has been explored [1].

The matched filter is essentially a cross-correlation filter in which the correlation function closely resembles the flaw signal. This correlation can be represented by the equation

$$g(m, n) = \sum_{i=1}^M \sum_{j=1}^N f(i, j) h(i - m, j - n) \quad (4.1)$$

where, $g(m, n)$ = filter output
 $f(i, j)$ = image
 $h(i, j)$ = filter
 (M, N) = size of kernel

The desired result of a matched filter is equivalent to maximizing the output SNR. The presentation of the following proof of the matched filter given here follows that of Stremler [27]. Considering stationary white noise with power density $\eta/2$, mean-square criteria can be applied to develop the impulse response of the matched filter. For the signal $f(t)$, a Fourier transform $F(f)$ is applied to a filter with frequency

response $H(f)$. The resulting output is $G(f) = H(f)F(f)$ with a Fourier transform

$$g(t) = \int_{-\infty}^{\infty} H(f)F(f)e^{j2\pi ft} df \quad (4.2)$$

At time t_0 , the signal magnitude is

$$|g(t_0)| = \left| \int_{-\infty}^{\infty} H(f)F(f)e^{j2\pi ft_0} df \right| \quad (4.3)$$

Therefore, the signal power at time t_0 is

$$S_p = |g(t_0)|^2 = \left| \int_{-\infty}^{\infty} H(f)F(f)e^{j2\pi ft_0} df \right|^2 \quad (4.4)$$

For white noise input, the average noise power at the filter output is

$$N_p = \frac{\eta}{2} \int_{-\infty}^{\infty} |H(f)|^2 df \quad (4.5)$$

Therefore, the SNR at filter output is

$$SNR = \frac{S_p}{N_p} = \frac{\left| \int_{-\infty}^{\infty} H(f)F(f)e^{j2\pi ft_0} df \right|^2}{\frac{\eta}{2} \int_{-\infty}^{\infty} |H(f)|^2 df} \quad (4.6)$$

The SNR can be maximized by applying the Schwartz inequality

$$\int_{-\infty}^{\infty} |u(x)|^2 dx \int_{-\infty}^{\infty} |v(x)|^2 dx \geq \left| \int_{-\infty}^{\infty} u(x)v(x) dx \right|^2 \quad (4.7)$$

For this case,

$$\int_{-\infty}^{\infty} |H(f)|^2 df \int_{-\infty}^{\infty} |F(f)|^2 df \geq \left| \int_{-\infty}^{\infty} H(f)F(f)e^{j2\pi ft_0} df \right|^2 \quad (4.8)$$

Substituting (4.8) into (4.6), the SNR may be simplified

$$SNR \leq \frac{\int_{-\infty}^{\infty} |H(f)|^2 df \int_{-\infty}^{\infty} |F(f)|^2 df}{\frac{\eta}{2} \int_{-\infty}^{\infty} |H(f)|^2 df}$$

$$SNR \leq \frac{2}{\eta} \int_{-\infty}^{\infty} |F(f)|^2 df \quad (4.9)$$

Since $|F(f)|^2 df$ is the energy of the signal (E), the maximum value for SNR occurs when $SNR = 2E/\eta$. Referring to the Schwartz inequality (4.7), the equation is equal when $v(x)$ is a proportional complex conjugate of $u(x)$, or $v(x) = ku^*(x)$. For this case, if $H(f)$ in (4.8) is replaced by

$$H(f) = kF^*(f)e^{-j2\pi ft_0} \quad (4.10)$$

the Schwartz expression becomes an equality, hence the SNR is maximized. Therefore, the impulse response with the same characteristics as the desired signal will maximize the SNR is

$$h(t) = k \int_{-\infty}^{\infty} F^*(f)e^{j2\pi ft_0} e^{j2\pi ft} df \quad (4.11)$$

or

$$h(t) = k f^*(t_0 - t) \quad (4.12)$$

In the specific case where the original signal $f(t)$ is real, the final result of the optimum filter is

$$h(t) = k f(t_0 - t) \quad (4.13)$$

Thus, the optimal filter will be a shifted and reversed version of the ideal signal, f . The shifting of the implies that the SNR is maximized when the filter is shifted to

the signal location. This derivation for a signal in time can be adapted spatially by replacing the variable t with the spatial coordinates (i, j) and t_0 with the spatial shift (m, n) . Hence for image applications, the original image has real values, thus the filter should be defined as

$$h(i, j) = k f(m - i, n - j) \quad (4.14)$$

Note that for correlation implementation, the optimal filter function is simply a shifted version of the ideal signal, f .

Results

The matched filter was tested on a series of images with known volumetric and crack-like flaws. For each case, test images were created using the x-ray simulation code developed by Gray et al. [12, 14, 15], then implemented on digitized radiographs acquired experimentally. Preliminary results were found using flat plate images with varying ellipsoidal flaw sizes, then complex geometry was considered using a more complicated part.

Volumetric Flaws

For a simple demonstration of the matched filter on different sized flaw, XRSIM was used to generate a series of flaws in a flat plate of aluminum. The flaws were modeled as voids, ellipsoidal in shape, constant in diameter, but with varying thickness of 1%, 3%, 5%, and 7% of the flaw diameter. Images were created at simulated generator settings of 50 keV and 1 mA-sec and are shown in Figure 4.1. In this series of images, only the 7% flaw is visible without processing.

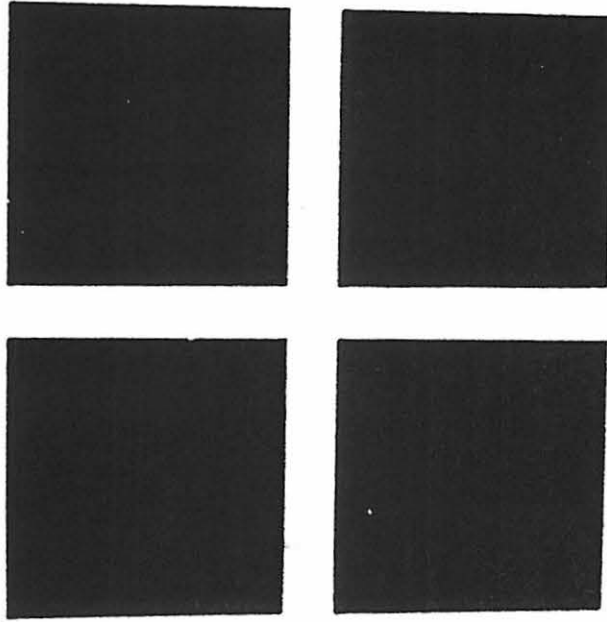


Figure 4.1: Original image of flat plate with voids. The flaw sizes clockwise from top left are 1%, 3%, 7%, and 5%.

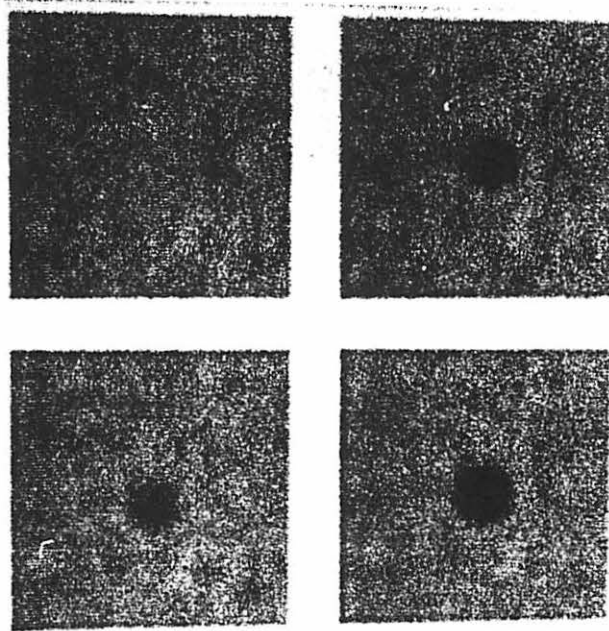


Figure 4.2: Filtered image of flat plate with voids. The flaw sizes clockwise from top left are 1%, 3%, 7%, and 5%.

A simple filter was used to process these images. Considering the circular shape of the flaw and disregarding the varying projected intensities due to the ellipsoidal shape, a basic cylinder with an amplitude of one was used in as a filter (11x11). This choice approximates the shape of the flaw, which enhances the signal, although not as optimally as an exact match. The impulse response for the matched filter used here was

$$h(i,j) = \begin{cases} 1 & r \leq 5 \\ 0 & r > 5 \end{cases} \quad (4.15)$$

The matched filter results are shown in Figure 4.2. The flaw signal in for the 3%, 5%, and 7% flaws were greatly enhanced by the matched filter. The 1% flaw was not improved in this case, because the flaw signal could not be distinguished from the background.

To quantify these results, the probability of detection (POD) was determined and a signal-to-noise ratio (SNR) was calculated before and after the filtering. The POD is a factor that quantifies on a scale of 0-1 whether or not a flaw can be detected [18]. The POD is 1 if the flaw is visually detectable and 0 if it is not detectable. Fractional PODs are possible and determined by considering the portion of observers that may see a marginally visible flaw. The SNR was calculated as

$$SNR = \frac{|m_{flaw} - m_{background}|}{\sigma_{background}} \quad (4.16)$$

where m_{flaw} is the mean value of a finite area of the the flaw signal, $m_{background}$ is the mean value of a same sized area in the background, and $\sigma_{background}$ is the

Table 4.1:

POD and SNR evaluation of Figures 4.1 and 4.2.				
Flaw Size	Original POD	Post-filter POD	Original SNR	Post-filter SNR
1%	0	0	0.1	0.16
3%	0.3	1	1.46	6.54
5%	0.6	1	2.60	9.54
7%	1	1	3.62	14.7

standard deviation of the background. Values for the POD and SNR of the images in Figures 4.1 and 4.2 are shown in Table 4.1.

As a next step, void detection in an actual digitized radiograph of a weld with 4 voids near the center of the image was considered. A (7x7) filter, similar in shape to the one described in (4.15), was used to process the image. The original and processed images are shown in Figure 4.3. The four voids in the weld are nicely enhanced by the matched filter. The original SNR for the four flaws were 3.48, 0.74, 0.77, and 0.64, from left to right, respectively. The SNR for the processed image were 34.34, 20.0, 10.3, and 15.16, respectively. Even though there was a significant SNR improvement for the smallest void, it is barely visible. It should be noted that it is difficult to capture a measure of the image quality with one number, such as SNR. Factors such as size shape, and the background have a profound effect on the detectability. Measures such as POD have the two-dimensional nature of images that better describes the response of a human viewing the image.

Since the filtering on the flat plate was successful, a complex part was considered. The different thicknesses in such a part appear as different shades of gray, with abrupt edges where the thickness changes. The air conditioner compressor part, shown in

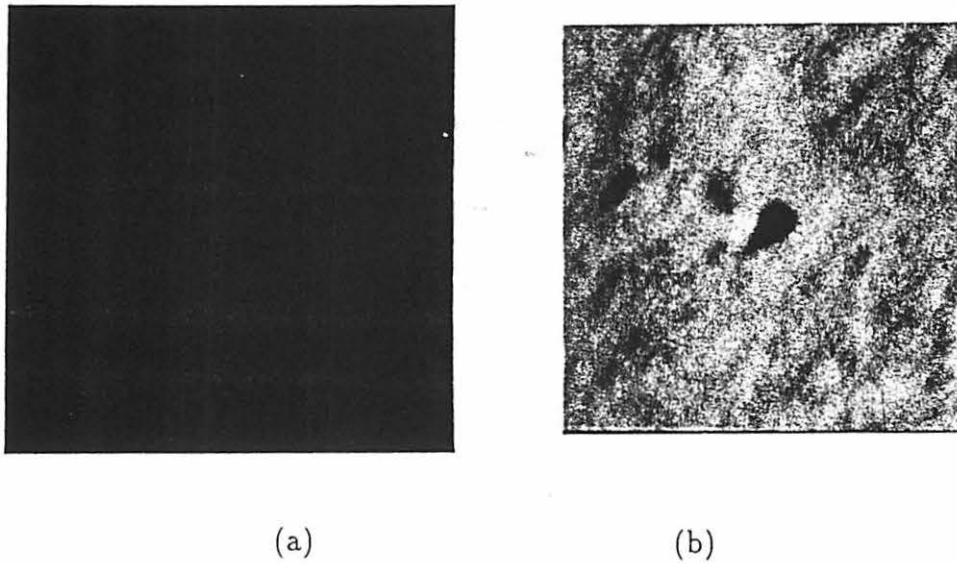


Figure 4.3: Detection of voids in an aluminum weld. (a) Original image. (b) Matched filter result.

Figure 2.3, was chosen for its varying geometry. This part was modeled with a volumetric flaw placed in its lower curved surface on the left (Figure 4.4). To create a filtering element, XRSIM was run with the same parameters, but without noise. The flaw area and location were known, so a 5x5 area at the center of the flaw was chosen, producing an asymmetric filter due to the background conformity. The values were reduced so that the minimum value was zero, thus retaining the shape, but minimizing the resulting range of values. The filter chosen for this application was

$$h(i,j) = \begin{bmatrix} 0 & 2 & 3 & 2 & 0 \\ 8 & 9 & 10 & 9 & 8 \\ 14 & 15 & 16 & 15 & 14 \\ 19 & 21 & 21 & 20 & 19 \\ 26 & 27 & 29 & 27 & 25 \end{bmatrix} \quad (4.17)$$

Using this filter on the original modeled image with noise, the matched filter result was found (Figure 4.5). The results were not as good as the flat plate examples, due to the varying background at the location of the flaw; however, the flaw signal was enhanced. Part of the reason the results do not appear very clearly in this example is that the image does not have a zero-mean. When the filter is run, the resulting image is a 16-bit image, which is difficult to display on a 256 gray scale.

SNR measurements could not be effectively calculated on these images because the nature of the image made it difficult to measure the noise. As an alternative way to illustrate the amplified flaw, a section around the flaw in each of the original and the processed image was plotted (Figure 4.6). The signal is not apparent in the noise

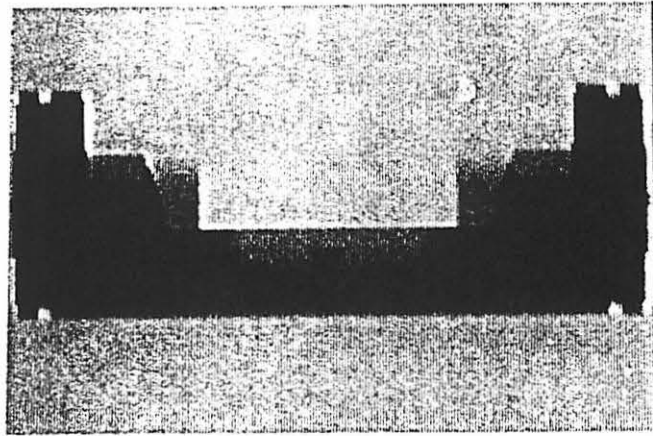


Figure 4.4: Original image of an air-conditioner part.

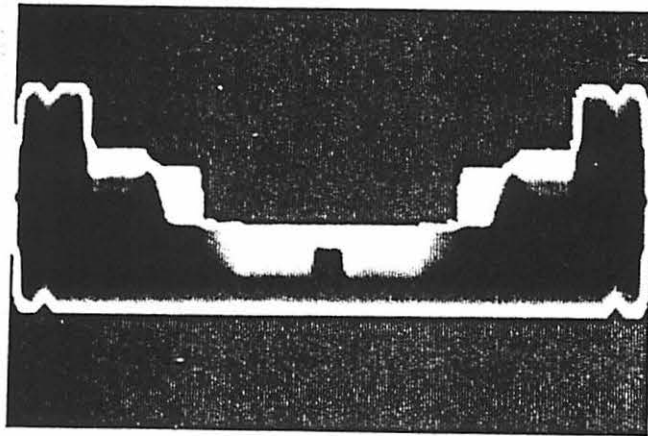
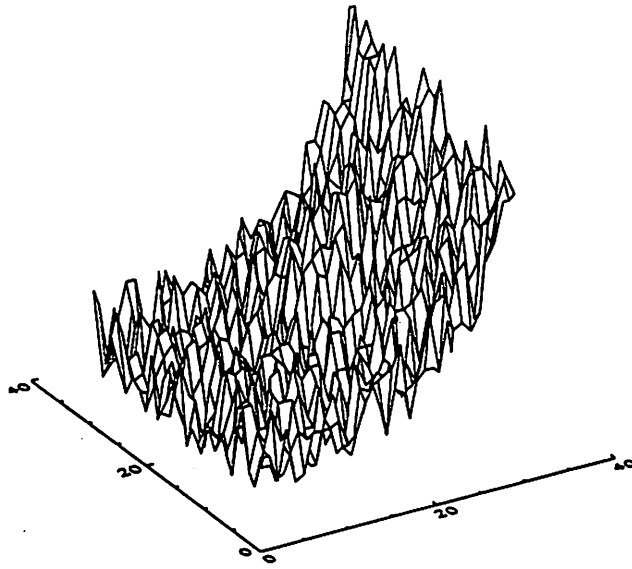
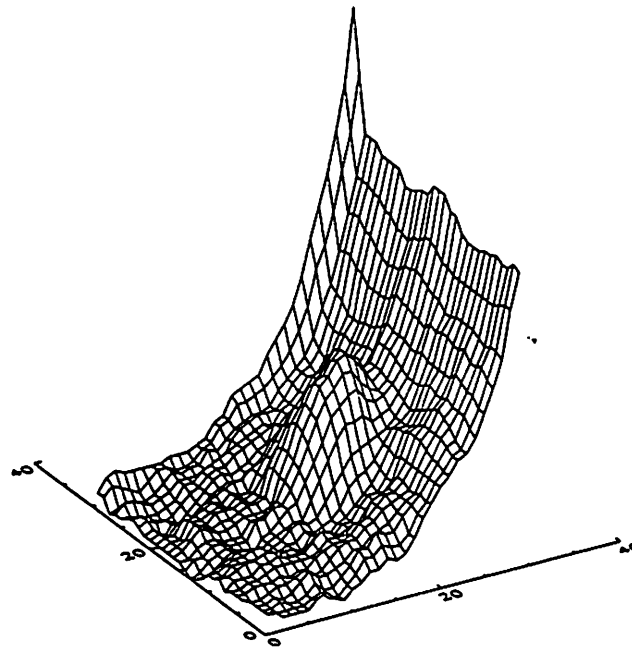


Figure 4.5: Filtered image of an air-conditioner part.



(a)



(b)

Figure 4.6: Plot of flaw area. (a) Original image. (b) Filtered result.

of the original image; however, the noise level has been reduced in the filtered image, revealing the flaw. It should be noted that the filter output of the background in this image becomes greater than that near the flaw, which inhibits the use of thresholding to better distinguish the flaw location in the image.

Crack-like Flaws

Work done by Chudhuri et al. [5] found that a series of filters could be used to achieve good results in locating retinal blood vessels. Since blood vessels are similar to cracks in shape, this idea was applied to locate cracks when orientation or type of flaw is unknown. These filters may be used separately, combining the results for a final image.

By creating some modeled images, the matched filter for cracks was examined. Cracks of different orientation were simulated in the image. Because cracks are generally one-dimensional, a filter representing a line was chosen, with a length sufficient to detect a signal. The filter for the cracks was a simple 7x7 filter with unity magnitude:

$$\begin{aligned} h(i, j) &= 0 \quad i \neq 3, \quad j = 0 \dots 6 \\ &= 1 \quad i = 3, \quad j = 0 \dots 6 \end{aligned} \quad (4.18)$$

This filter was used and rotated through several angles to detect cracks in several different orientations (Figure 4.7). Figure 4.8 shows the result of simply summing the images after each filter pass. In summing the series of filtered images, the flaws are located but not well defined. It was found that the process worked best if a threshold was taken after each filter was run to isolate the amplified results. This result is shown in Figure 4.9. This extended the processing time, but gave considerably better

results.

Real radiographs were also examined. An image of an aluminum weld was considered. The nature of the image, a straight vertical crack in a flat field, made it an ideal candidate for just one pass of the slit filter. The crack was nicely amplified, with the crack clearly shown in Figure 4.10. The SNR of the original image was 3.46; however, the processed SNR was 8.37. The vertical streaking in the processed image is an artifact of the filtering process, but does not detract from the overall result.

Another radiograph was examined, which was an image of damage around a bolt hole. This image was chosen because it was true representation of damage that might occur during assembly or in-service. Although the bolt hole is not actually shown in this image, Figure 4.11 show several small cracks radiating from the hole. The large amount of gray scale variation in the background caused the filter missed many of the true features, but gave a decent representation of some of the image structure. The attempt was most likely unsuccessful because of the background variation.

Summary

The matched filter works ideally by reducing the noise and boosting the desired signal, effectively enhancing the flaw or structure. It was shown that the POD and SNR could be significantly increased by using the matched filter. Matched filters are an effective way to extract volumetric and crack-like flaws from high noise, flat-field images. Although not all objects of interest are flat plates, some images have fairly simple trends which can be removed to approximate a flat plate. A series of matched filters may then be run on the new image to further enhance the flaws.

The filters enhance the signal to noise ratio in an image by using a filter element

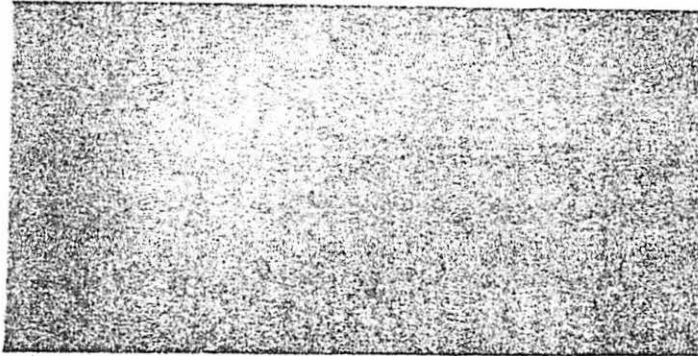


Figure 4.7: Model generated image with cracks.

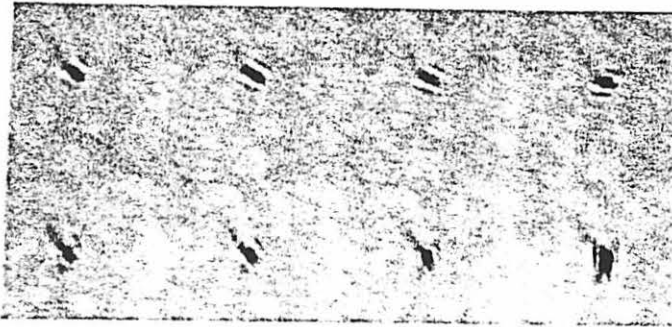


Figure 4.8: Filtered with passes at several different angles.



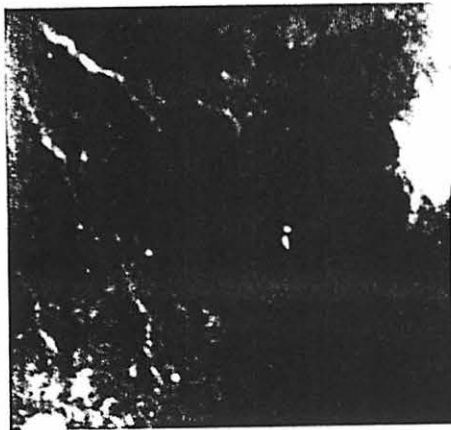
Figure 4.9: Filtered image with thresholded images summed.



(a)

(b)

Figure 4.10: Crack in weld. (a) Original image. (b) Filtered result.



(a)



(b)

Figure 4.11: Image near bolt-hole. (a) Original image. (b) Filtered result.

that closely matches the shape and size of the actual flaw. While it is difficult to design a filter that will exactly match a specific flaw, it is possible to create a general filter that will locate the specific flaw. The approximate filter shape can be determined and the size estimated from inspection criteria. Most of the time, the flaw morphology is known when designing inspection procedures. For example, in-service inspection may focus on cracks due to fatigue damage, while a defects in manufacturing would more likely be volumetric porosity.

Generally, the filter size should correspond with the expected flaw size. For this work, a 7x7 filter was considered a reasonable size; however, it is difficult to recommend a general size for a filter, because the sizing is relative to the expected flaw in a specific image. For initial trials in determining the size of a filter, it is better to keep the filter simple and under size the flaw geometry because it will still correlate with the flaw, but not give the optimal response. If the filter is too small, it may correlate with other features in the image, creating a distorted result. If the filter is too large, it may not correlate with any of the features in the image.

The choice of shape of a filter can be fairly simplistic. If a void is the feature of interest, a circular or area type filter should be used. Conversely, if a crack is the feature of interest, a linear type filter should be used. The complexity comes in optimizing the magnitude and form of the filter to optimize the results. Crack detection also requires that several angles be considered by cycling through a series of orientations to match a crack. For this work, an increment of 5 degrees was used.

When choosing the amplitude of the filter values, an attempt should be made minimize the values of the filter, while retaining its shape. The mean of the filter affects the dynamic range of the resulting image, which will cause problems when

trying to display the image. When the resulting data values from the matched filter are greater than the 256 gray scale values available to display the image, it is difficult to extract the flaw information. If the image was scaled to fit the 8-bit display, information related to the dynamic range of the filtered result was lost. A system to more effectively view selected gray scale portions of 16-bit data would be necessary to evaluate the filter results. Alternatively, it may be desirable to simply create a zero-mean filters, so that the resulting image is on the same order as the original image.

Although the matched filter was not very effective on an image with a varying background, there are many applications in NDE that require inspections of objects with flat field backgrounds or with trends that are easily removed. The matched filter would be very useful in these applications. The technique is simple, fast, and provides a mode to identify flaws which might initially be missed.

CHAPTER 5. IMAGE SUBTRACTION

Image subtraction is a technique used for comparing similar images. Subtraction removes unwanted image features, revealing and isolating features of interest. It is frequently used in medical applications to observe growths, by comparing the changes over time [11]. Subtraction can also be used to remove bone structure, which is done by taking radiographs at two different energies. It has also been used in machine vision applications as a pattern recognition and sorting tool [28].

In this study, it was desired to remove features in radiographs related to thickness variations in a part. This has two consequences if it can be done successfully. The first is to provide a stationary background for further processing by the matched filter. The second is a simpler image for interpretation by a radiographer. In the first case, the level of artifacts left must be very low. In the later case, this requirement is less stringent. A simulated radiograph of a non-flawed, or ideal part can be created using XRSIM, then compared to a radiograph of an actual part. By subtracting the ideal radiograph from the real, the effects of the thickness variations are reduced and otherwise undetectable flaws are revealed. This process effectively replaces the need for multiple radiographs for thick and thin regions of a part, thus reducing inspection time and cost. This is especially useful in automated inspection for a production situation where the same type of part is repeatedly being inspected.

Since the images are produced by different modes, some consideration must be taken that the part is similarly represented in both images. The gray scale registry, spatial registry, and size of the images must closely correspond to result in a good subtraction. The gray scale registry is a calibration between the values of a digitized radiograph and the values generated by XRSIM. Spatial registry refers to the adjustment in orientation of the images. Size refers to the pixel dimension of the image, because the images must be of the same order to subtract.. Details and results of the subtraction process are presented in this chapter.

Calibration

When working with digitized radiographs, it must be kept in mind that there are two different ways to quantify the gray shades on the radiograph: optical density values of the actual radiograph and gray scale values of the digitized image. The optical density values usually range in real numbers from 0 to 5, where 0 is white and 5 is black. On the other hand, digital gray scale values are typically limited to 8-bit information contained in the 0-255 gray scale, where 0 is black and white is 255. The relationship between these two scales is highly dependent upon the parameters of digitization, as it was described in Chapter 3.

For the image subtraction performed in this work, a simulation result from XRSIM and the experimentally generated image are compared. It is important that the two images, created by different modes, are calibrated. To verify that XRSIM was producing optical density values comparable to actual radiograph density values, a radiograph of an aluminum step wedge was taken and its density values compared to the XRSIM values for the same range of aluminum thicknesses. The model generated

values compared well with actual density values. Figure 5.1 illustrates the comparison of the film densities measured and the XRSIM calculated values for varying thicknesses of aluminum at the same experimental setting.

The densities produced by XRSIM are good representations of the actual film response, but the corresponding gray scale values did not match the digitized values. XRSIM was written with a linear conversion between optical density values and gray scale values. As was shown in Figure 3.2 and 3.3, this relationship is not linear. The gray scales for the model generated densities were adjusted by altering the film parameters in XRSIM to closely match the values produced by the digitization system at particular settings. A comparison of the gray scale mapping for the two methods is shown in Figure 5.2. The adjusted parameters were then used to generate the gray scale images used in subtraction. In this way, the effect of the digitization chosen was modeled. The original film model in XRSIM included only the film response. Modification to the parameters allow the effect on the model response of the lightbox, camera, and frame grabber to be included. This allowed a common currency, gray scale, to be used to perform the unique subtraction.

This gray scale calibration is necessary to get a good correspondence between the intensities of the images. It should be noted that this calibration will change with each new setting of any parameter of the digitization system. If just one group of settings is used for all digitization purposes, a library of specific calibrations could be created and the appropriate setting selected as needed.

Although it was not done in this work, a better way to adjust this calibration would be to utilize calibration curves, such as the ones shown in Figure 3.2. This calibration information could be used to transform the density values of XRSIM to

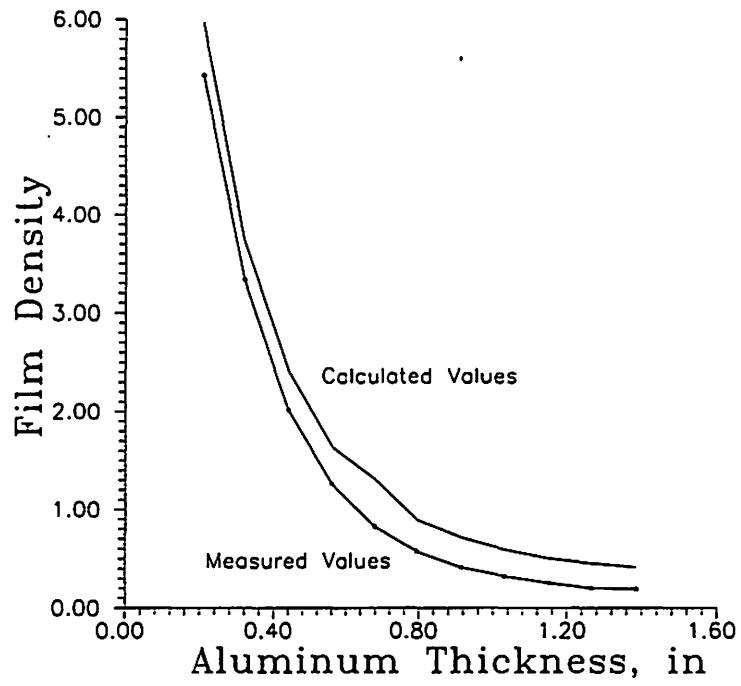


Figure 5.1: Density comparison of model output to measured values.

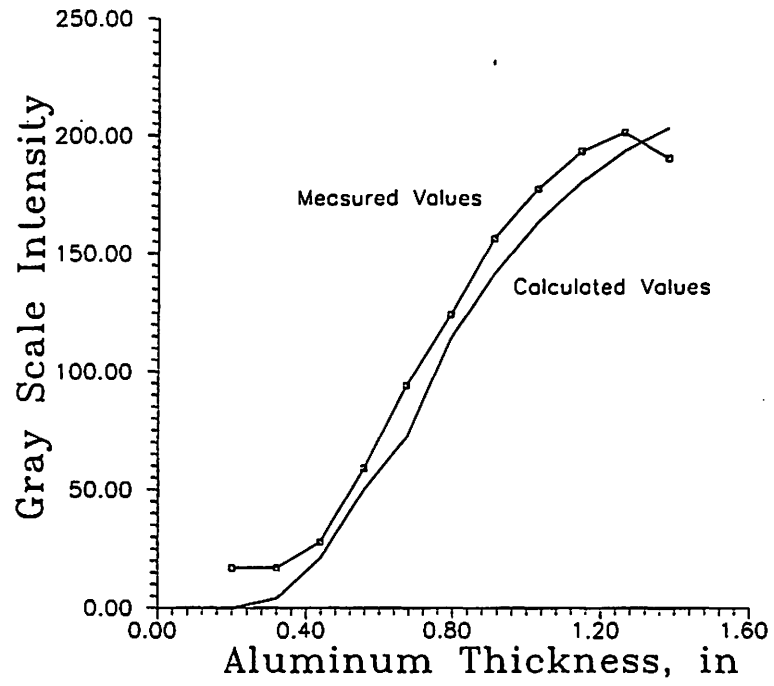


Figure 5.2: Gray scale calibration for model output.

matched the digitized values of the radiograph. Conversely, a better approach would be to maintain the density values generated by XRSIM and use the digitization calibration curves to convert the gray scale values of the digitized radiograph, back to density values, thus retaining a larger dynamic range of information.

Image Registration

Spatial registration of the images is necessary before subtracting two images. There are several different methods for adjusting orientation, which vary in complexity and interactivity. One technique simply uses control points, which are chosen to mark corresponding features on both images, then a geometric transformation is used to estimate the new position [3]. Another method uses complex image moments, which are normalized to a reference position. There is also a method that uses the image edges for registry, for which the intensity of the edge pixels are compared and a geometric transformation is found [11].

A method utilizing control points was chosen for this work, because it was a simple method that worked well. The control points were selected manually, by marking easily identifiable features on the original object and extracting the coordinates. The corresponding features were then marked and coordinates extracted from the model generated image. Based on experience, it was found that at least 6 sets of points were necessary to obtain reasonable results. A least squares approximate was then used to obtain the matrices for the affine transformation. The image spatial registry was then corrected using the calculated affine transform to warp the model-generated image to the size and orientation of the real image.

An affine transform adjusts for translation, scale, and rotation of the image,

while preserving straight lines, parallelism, and scale homogeneity [25]. To transform a 2-D image function in the form $f(\underline{x}) = f(x_1, x_2)$, the general affine transform can be expressed as

$$f'(\underline{x}) = f(\underline{x}') \quad (5.1)$$

where,

$$\underline{x}' = A\underline{x} + \underline{b} \quad (5.2)$$

A is defined as the homogeneous affine transform matrix and \underline{b} is the translation vector:

$$\begin{bmatrix} x'_1 \\ x'_2 \end{bmatrix} = \begin{bmatrix} a & b \\ c & d \end{bmatrix} \begin{bmatrix} x_1 \\ x_2 \end{bmatrix} + \begin{bmatrix} b_1 \\ b_2 \end{bmatrix} \quad (5.3)$$

There are 3 basic transformations, which can be combined to give the desired result:

$$A = \begin{bmatrix} \alpha & 0 \\ 0 & \alpha \end{bmatrix} \quad b = \begin{bmatrix} 0 \\ 0 \end{bmatrix} \quad \text{magnification} \quad (5.4)$$

$$A = \begin{bmatrix} \cos\theta & -\sin\theta \\ \sin\theta & \cos\theta \end{bmatrix} \quad b = \begin{bmatrix} 0 \\ 0 \end{bmatrix} \quad \text{rotation through origin by angle } \theta \quad (5.5)$$

$$A = \begin{bmatrix} 1 & 0 \\ 0 & 1 \end{bmatrix} \quad b = \begin{bmatrix} \Delta x_1 \\ \Delta x_2 \end{bmatrix} \quad \text{translation } (\Delta x_1, \Delta x_2) \text{ in } (x_1, x_2) \quad (5.6)$$

For the cases explored in this work, it was desired to transform an image to register into another image for subtraction. By sampling corresponding points on the real and modeled images, A and \underline{b} were determined using a least square fit, then used to transform the modeled image. The modeled image was then subtracted from the real image.

Even with the two images spatially aligned, the subtraction may have edges or areas which do not match, because of the differences between the actual part and

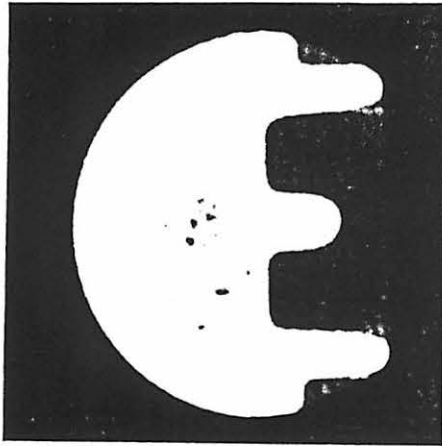
the CAD model. As noted in Chapter 2, a modeled part may not have the rounded edges of the real part. Upon subtraction, this difference will produce an edge effect where the images do not correspond. The level of fidelity of the CAD model to the part will depend upon the strength of the need for image registry.

To illustrate the image registry technique and the image mismatch due to the CAD model, a subtraction was performed on computed tomography (CT) images of the part shown in Figure 2.3. These images were chosen because they represent a zero-thickness radiographic image, which illustrates the point of image registry, without complicating matters with the thickness effect. Ten points unique to the geometry of the image were selected and manually sampled on each image. The corresponding points were the six "corners" of the object, the center edge of the three "prongs", and the center edge of the rounded arch. These points were then used in a least squares algorithm to determine the transform:

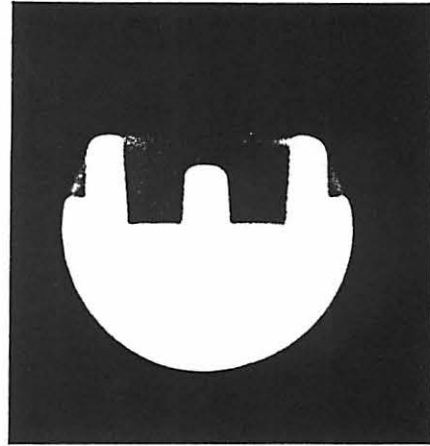
$$A = \begin{bmatrix} 0.0321592 & -0.742488 \\ 0.747240 & -0.227243 \end{bmatrix} \quad b = \begin{bmatrix} 37.6965 \\ 226.055 \end{bmatrix}$$

The simulated CT slice was transformed to match the real image, then subtracted. The image of an experimental CT reconstruction, a model generated CT slice of the same region, and the result is shown in Figure 5.3. The nearly uniform gray field of the image means that match is very close. The light and dark regions at the edges of the part show where the CAD model fails to meet the actual part.

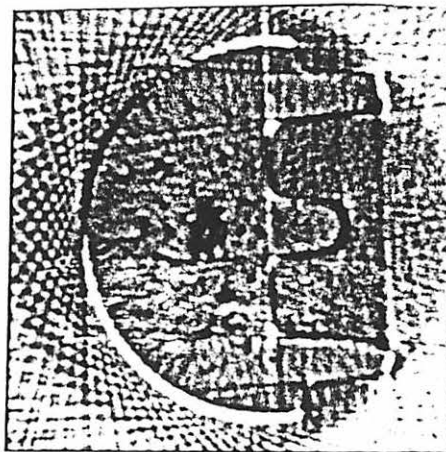
It is assumed that the orientations of the part and its modeled counterpart can be closely approximated. Since the objects are three-dimensional, being projected onto two-dimensional media, there is additional room for error if the pitch of one does not match the other. This factor is assumed to be negligible; an assumption



(a)



(b)



(c)

Figure 5.3: (a) Original CT image. (b) Model generated image. (c) Subtracted image.

which experience confirmed.

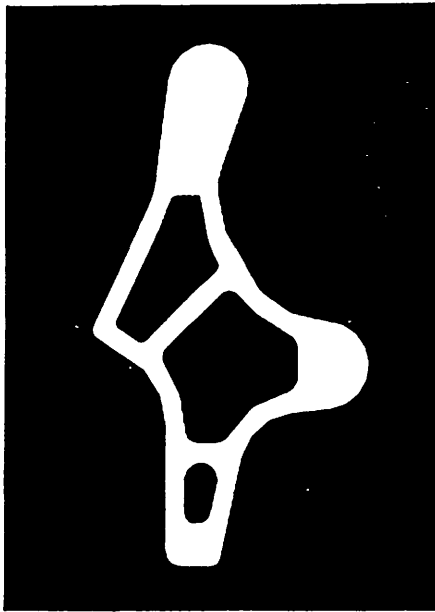
Subtraction

Image subtraction is a simple mathematical process performed on the pixels of an image. For two similar images of the same size, the pixel values of one image are subtracted from each corresponding pixel on the other image. Hence, an ideal image can be subtracted from a flawed image revealing differences in the images. Theoretically, the subtraction results in an image of a nearly uniform field, except for the dissimilarities present in the images.

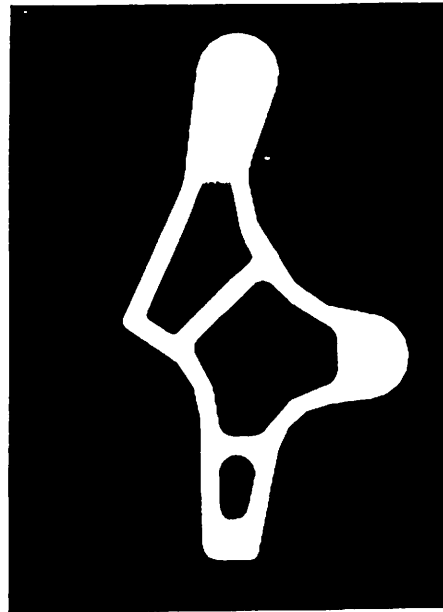
The subtraction process under ideal circumstances can be illustrated using XRSIM. Figure 5.4 depicts an arbitrary part that was chosen and modeled. Using the same parameters and the flaw feature of XRSIM, an ellipsoidal void was placed at a section of varying material thickness at the top of the part. Since this flaw is small in proportion to the thickness of the part and located on a non-uniform background, it is not readily seen in the simulated radiograph. However, when the images are subtracted and rescaled to enhance contrast, the flaw appears vividly on a blank background.

This example works very well because the images were generated in exactly the same manner, thus were identical except for the selected variable of the flaw. In this example, there is no problem with image registration; however, if two radiographs were experimentally taken of similar parts, there could possibly be some misregistration in the orientation of the parts, because the radiographs may not be in precisely the same position upon digitization. If the images are not aligned for subtraction, the anomalies in registration will also be shown.

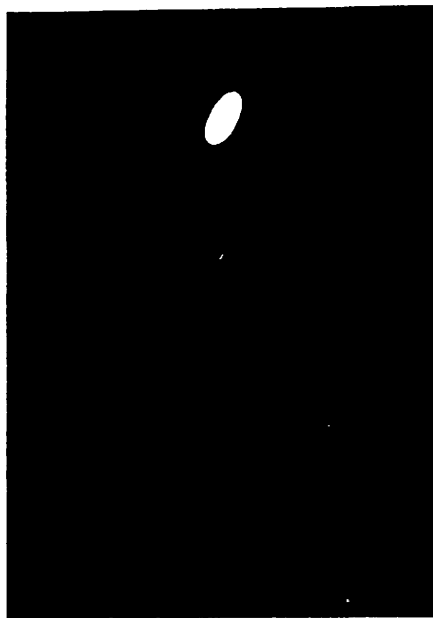
(1)



(a)



(b)



(c)

Figure 5.4: Arbitrary cast part. (a) Model generated image with flaw. (b) Model generated image without flaw. (c) Subtracted image.

Extending this method to incorporate real radiographs, the part shown in Figure 2.3 was used as an example of a part with complicated geometry. Because the edge portion of the has several thicknesses and geometries, it was chosen to exemplify the subtraction process. The CAD file representing the same part was used as input to the x-ray measurement model to produce an image resembling a radiograph, based on the same parameters as used experimentally. Although the real and simulated images appear to be fairly well registered to each other, corresponding points on the images were selected and a transform found to reposition the simulated image. For this case, the transfer variables are

$$A = \begin{bmatrix} -1.01255 & 0.0062411 \\ -0.0198319 & 1.09470 \end{bmatrix} \quad b = \begin{bmatrix} 1.84671 \\ -14.5757 \end{bmatrix}$$

The model generated image was then subtracted from the real image. Figure 5.5 shows the real, simulated, and subtracted images. Although some shrink porosity is visible in the original image, these flaws are better defined in the subtracted image.

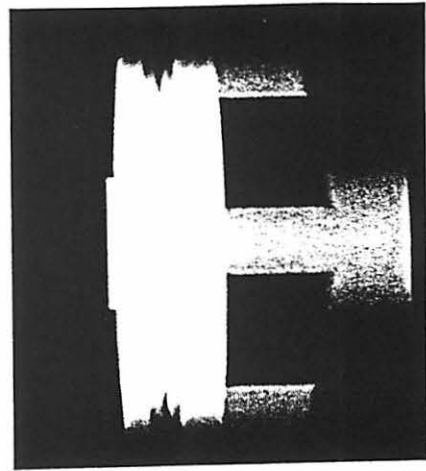
Another example is shown in Figure 5.6. The digitized radiograph shows visible flaws in some of the thicker portions of the part, but leaves the remainder of the image in a nearly black field. For comparison, a model generated reference image of the same portion is created using the same experimental settings. After registering and subtracting the images, details of the part's anomalies are shown. The modeled image was transformed using

$$A = \begin{bmatrix} -1.00750 & 0.00909622 \\ 0.000824525 & 1.01081 \end{bmatrix} \quad b = \begin{bmatrix} -1.17119 \\ -3.74033 \end{bmatrix}$$

In the resulting image, two features are of interest. A crack which originates in the thick portion of the part and is visible in the original image, actually continues into



(a)



(b)



(c)

Figure 5.5: Edge section of air-conditioner part. (a) Digitized radiograph. (b) Model generated image. (c) Subtracted image.

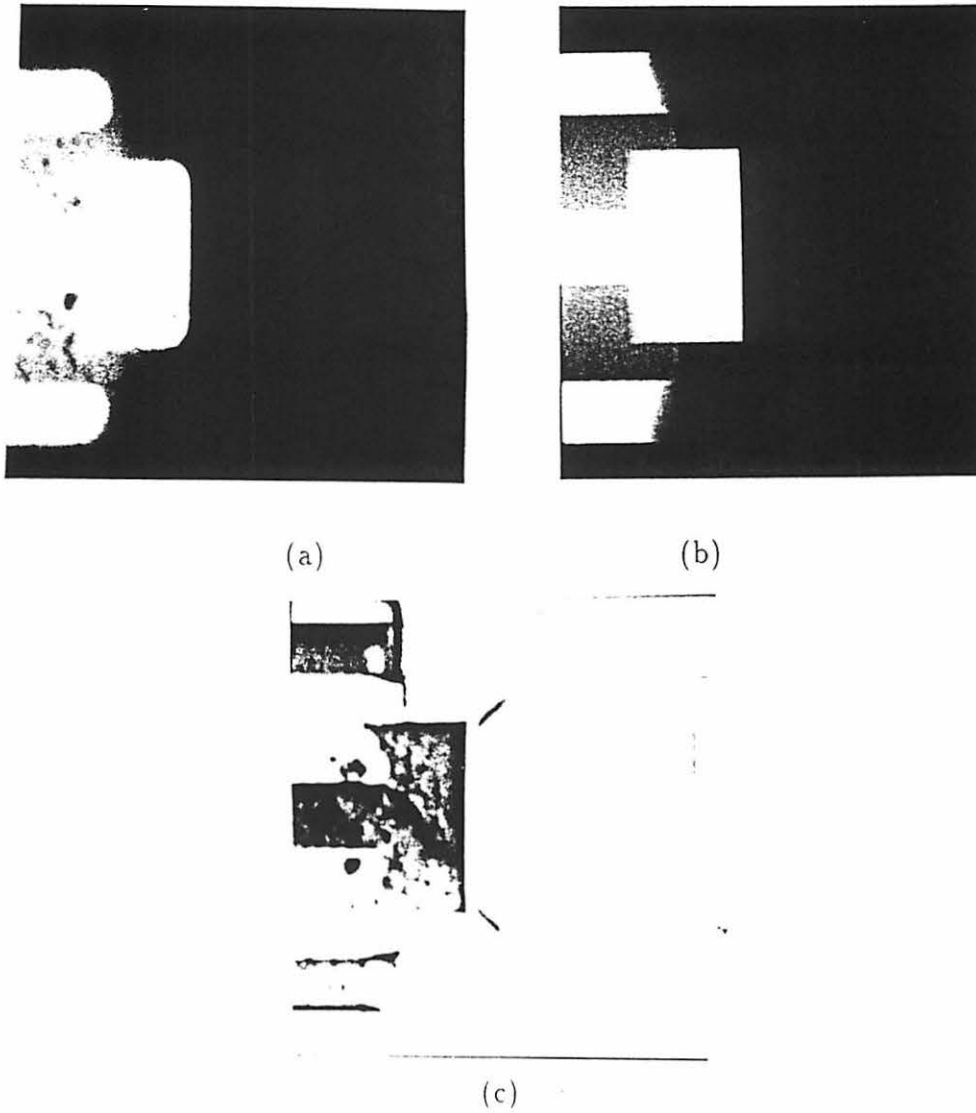


Figure 5.6: Center section of air-conditioner part. (a) Digitized radiograph. (b) Model generated image. (c) Subtracted image.

the thinner portion of the part which was previously black. Without the subtraction, the crack would have been under sized by 30%. Another feature that is revealed is the "3" near the center of the image, which is a raised number marking on the actual part. Although this is not a flaw per se, it is a small variation in material thickness which was not detectable on the original image.

Some error remains in the process, even with the corrections for the orientation and digitized pixel intensity calibration. As previously mentioned, there is some mismatch between the contours of the actual part and the CAD model; however, this can be corrected. Also, an error may occur if the material of the casting was not the same alloy as assumed for the model; the x-ray absorption coefficient would differ, resulting in slightly different film densities. Adjustments for these factors will result in better subtracted images.

Summary

In this study, the main goal of the image subtraction was to minimize the part geometry to reveal flaws otherwise undetectable. Often with parts of complicated geometry where the thicknesses vary greatly, several exposures are necessary to successfully inspect the entire part. Considering the part shown, a portion was chosen with several thicknesses and geometries. The digitized radiograph shows some of the flaws in the thicker portions, but leaves the remainder of the image in a nearly black field. By transforming and subtracting the same portion of a simulated image, more details of the part's anomalies are shown. The flaws are enhanced in the thicker portion, fully revealing a crack that originates in the thick portion and runs into the thinner portion (previously dark). Another detail that should be noted is the "3"

near the center of the image, which is a raised number marking on the actual part.

Even with the corrections for the orientation and digitized pixel intensity calibration, the subtractions are not ideal. While the darker gray portion may indicate an error in intensity calibration, it may also indicate an error in the process model itself. If the material of the casting was not the same alloy assumed during the modeling process, the x-ray absorption will differ, resulting in slightly different film densities. As the process model is refined, this effect should diminish. In summary, the subtraction process, while imperfect can definitely aid an inspector in identifying and sizing flaws.

CHAPTER 6. CONCLUSIONS

This work explored the use of image processing techniques for the specific purpose of flaw detection in radiographs. It was desired to utilize the information regarding the generation of x-ray radiographs to improve the probability of detecting flaws in radiographs. Since the x-ray simulation code (XRSIM) was available to generate information about specific parts and x-ray images, its usefulness as a tool for image processing was explored. Application specific techniques were developed by utilizing the information available about the part and its inspection criteria.

The two techniques examined used XRSIM, yet took different approaches to feature extraction. The matched filter technique utilized the flaw feature of XRSIM to design appropriate filters to enhance particular critical flaws. Whereas, the image subtraction technique was used to suppress the geometric features of the part, which obscured the flaw features.

It was expected that the filters created using XRSIM would significantly boost the signal of the flaw; however, these filters were no more successful than the simply derived filters. It was found that the simple filters that worked well, reasonably approximated the shape and were not over sized. In fact, it was shown that filters smaller than the flaw did a good job of matching and locating the slightly larger flaws. Although the matched filter technique did not work as expected, it did show

some promising results for limited applications. The detectability of volumetric flaws in both a flat plate and a complex geometry parts were both enhanced using the matched filter. Crack-like flaws were also detected using a series of filters to account for the many possibilities in orientation.

One of the problems that occurred with this technique was that the resulting data values from the matched filter were greater than the 256 gray scale values available to display the image. If the image was scaled to fit the 8-bit display, information related to the dynamic range of the filtered result was lost. This caused difficulties in evaluating the results, simply because there was not a simple way to view the data. A system to more effectively view selected gray scale portions of 16-bit data is currently being developed.

Although the matched filter is not very effective on an image with a varying background, the technique is not so limited that it unusable. Examination of Figure 4.6 shows a significant enhancement of a flaw on a varying background. The display of this image on an 8-bit gray scale, resulted in a loss of most of the detail. On the other hand, there are many applications in NDE that require inspections of objects with flat field backgrounds or with trends that are easily removed. Because the nature of the defects and inspection criteria are usually known, filter elements representing the shape and size of the flaw can be created.

Image subtraction was used to reduce the effects of the part's physical geometry. This would reduce the need for several exposures to successfully inspect the part with multiple thicknesses. The technique worked quite well, revealing flaws that were otherwise difficult to see. Although the image match was not perfect because the dual origins of the images, the results revealed image features that were not

previously apparent.

The potential of using image subtraction as a method to eliminate need for multiple radiographs is significant. Considering that a medium size casting company will have 3000 parts to inspect each month, requiring 2-3 radiographs per part. The cost of film, developing, and labor may be range between \$4-\$6 per radiograph. By implementing image subtraction, the savings in reduction of film costs can pay for the system in several months.

In developing these techniques, it was observed that information on digitization and dynamic range is important to consider when processing images. The processing techniques will be most effective when the maximum amount of information be available. Care must be taken in digitizing the radiographs so that the amount of data collected is optimized. If the data is not complete, it is difficult to manipulate it.

Future Work

Some work is still necessary to refine the calibration between the calculated densities of XRSIM to the actual gray scale values used for imaging. As mentioned in Chapter 3, there are several different ways to digitize a radiograph and use its information. In order for the image subtraction to be valid, a corresponding calibration curve would be necessary for any possible digitization configuration. This can be simplified by choosing standards.

The concept of dynamic range expansion may also be explored. Better control of the lightbox is necessary for repeatability of the settings. A custom lightbox with digital control might be built to have consistent illumination. By having better

control of the digitization process, the digitized images might be remapped to their original density values and compared directly to the XRSIM density outputs.

Another possible step is to expand the image subtraction concept to real-time imaging. The real-time model is not yet complete, however, this would be a natural extension of the technique. It may have better use in this form, since it would remove the digitization process and work directly with the output from an image intensifier.

REFERENCES

- [1] R.A. Boie, I.J. Cox, and P. Rehak. On Optimum Edge Recognition Using Matched Filters. *IEEE Proc. Conf. Computer Vision Pattern Recognition*, June 22-26, 1986: 100-108.
- [2] A.C. Bovik, T.S. Huang, D.C. Munson, Jr. The Effect of Median Filtering on Edge Estimation and Detection. *IEEE Trans. PAMI.*, Vol. 9, No. 2, March 1987: 181-194.
- [3] L.G. Brown. A Survey of Image Registration Techniques. *ACM Computing Surveys*, Vol. 24, No. 4, December 1992: 325-376.
- [4] H.M. Burte and D.E. Chimenti. Unified Life Cycle Engineering: An Emerging Design Concept, *Review of Progress in Quantitative Nondestructive Evaluation*, Vol. 6B, D.O. Thompson and D.E. Chimenti, eds. New York: Plenum Press; 1987: 1797-1809.
- [5] S. Chaudhuri, S. Chatterjee, N. Katz, M. Nelson, and M. Goldbaum. Detection of Blood Vessels in Retinal Images Using Two Dimensional Matched Filters. *IEEE Transactions on Medical Imaging*, Vol. 8, No. 3, 1989: 263-269.
- [6] D.B. Cooper and F.P. Sung. Multiple-Window Parallel Adaptive Boundary Finding in Computer Vision. *IEEE Transactions PAMI*, Vol. 5, No. 3, May 1983: 299-316.
- [7] P.R. Detmer, G. Bashein, and R.W. Martin. Matched Filter Identification of Left-Ventricular Endocardial Borders in Transesophageal Echocardiograms. *IEEE Transactions on Medical Imaging*, Vol. 9, No. 4, December 1990: 396-404.
- [8] J. Dunlop and D.G. Smith. *Telecommunications Engineering*, Berkshire, England: Van Nostrand Reinhold; 1984: 145-148.

- [9] Eastman Kodak Co. *Radiography in Modern Industry*, 4th ed. Rochester, NY: 1980.
- [10] M. Foley and J.N. Gray. A Computer Simulation Model for X-Ray Computed Tomography, presented at the *Review of Progress in Quantitative Nondestructive Evaluation*, University of California-San Diego, La Jolla, CA, July 19-24, 1992.
- [11] P. Gerlot-Chiron and Y. Bizais. Registration of Multimodality Medical Images Using a Region Overlap Criterion. *CVGIP: Graphical Models and Image Processing*, Vol. 54, No. 5, September 1992: 396-406.
- [12] J.N. Gray. Three Dimensional Modeling of Projection Radiography, *Review of Progress in Quantitative Nondestructive Evaluation*, Vol. 7A, D.O. Thompson and D.E. Chementi, eds. New York: Plenum Press; 1988: 343-348.
- [13] J.N. Gray, T.A. Gray, N. Nakagawa, and R.B. Thompson. Models for Predicting NDE Reliability, *Electronic Materials Handbook, Volume 1: Packaging*. Materials Park, OH: ASM International: 1989.
- [14] J.N. Gray, F. Inanc, and B.E. Shull. Three Dimensional Modeling of Projection Radiography, *Review of Progress in Quantitative Nondestructive Evaluation*, Vol. 8A, D.O. Thompson and D.E. Chementi, eds. New York: Plenum Press; 1989: 345-350.
- [15] J.N. Gray and F. Inanc. A CAD Interfaced Simulation Tool for X-ray NDE Studies, *Review of Progress in Quantitative Nondestructive Evaluation*, Vol. 9A, D.O. Thompson and D.E. Chementi, eds. New York: Plenum Press; 1990: 391-398.
- [16] J.N. Gray. Personal communication.
- [17] J.N. Gray, T.A. Gray, N. Nakagawa, and R.B. Thompson. Models for Predicting NDE Reliability, *Metals Handbook*, 9th Edition, Vol. 17, Materials Park, OH: 1989.
- [18] J.N. Gray, T. Jensen, and R.M. Wallingford. Application of an X-Ray Process Model for Inspection Optimization, *Review of Progress in Quantitative Nondestructive Evaluation*, Vol. 12A, D.O. Thompson and D.E. Chementi, eds. New York: Plenum Press; 1993: 319-327.
- [19] R. Halmshaw. *Non-destructive Testing*. London, England: Edward Arnold; 1987.
- [20] C.J. Jacobus and R.T. Chien. Two New Edge Detectors. *IEEE Transactions PAMI*, Vol. 3, No. 5, September 1981: 581-592.

- [21] A.K. Jain. *Fundamentals of Digital Image Processing*, Englewood Cliffs, NJ: Prentice Hall; 1989.
- [22] R. Machuca and A.L. Gilbert. Finding Edges in Noisy Scenes. *IEEE Transactions PAMI*, Vol. 3, No. 1, January 1981: 103-111.
- [23] D.O. North. Analysis of the Factors which Determine Signal/Noise Discrimination in Radar. *RCA Laboratories, Princeton, NJ Rept. PTR-6C*, June 1943.
- [24] L. O'Gorman and J.V. Nickerson. Matched Filter Design for Fingerprint Enhancement. *IEEE International Conference on Acoustics, Speech and Signal Processing*, 1988: 916-919.
- [25] R.J. Schalkoff. *Digital Image Processing and Computer Vision*, New York: Wiley, 1989.
- [26] W.A.C. Schmidt. Modified Matched Filter for Cloud Clutter Suppression. *IEEE Transactions PAMI*, Vol. 12, No. 6, June 1990: 594-600.
- [27] F.G. Stremler. *Introduction to Communication Systems*, Reading, MA: Addison-Wesley; 1990.
- [28] C.L. Su. *Techniques for Image Registration and Image Subtraction for Industrial Inspection*. M.S. Thesis, University of Louisville; 1987.
- [29] G.L. Turin. An Introduction to Matched Filters. *IRE Transactions Information Theory*, Vol. IT-6, No. 3, June, 1960: 311-329.
- [30] G.L. Turin. An Introduction to Digital Matched Filters. *Proceedings IEEE*, vol. 64, July 1976: 1092-1112.
- [31] K.W. Ulmer. *Automated Flaw Detection Scheme for X-ray Image in Nondestructive Evaluation*. M.S. Thesis, Iowa State University; 1992.